

MIT Open Access Articles

Solar steam generation by heat localization

The MIT Faculty has made this article openly available. **Please share** how this access benefits you. Your story matters.

Citation: Ghasemi, Hadi, George Ni, Amy Marie Marconnet, James Loomis, Selcuk Yerci, Nenad Miljkovic, and Gang Chen. "Solar Steam Generation by Heat Localization." Nature Communications 5 (July 21, 2014).

As Published: <http://dx.doi.org/10.1038/ncomms5449>

Publisher: Nature Publishing Group

Persistent URL: <http://hdl.handle.net/1721.1/95979>

Version: Author's final manuscript: final author's manuscript post peer review, without publisher's formatting or copy editing

Terms of Use: Article is made available in accordance with the publisher's policy and may be subject to US copyright law. Please refer to the publisher's site for terms of use.



Solar Steam Generation by Heat Localization

Hadi Ghasemi, George Ni, Amy Marie Marconnet, James Loomis, Selcuk Yerci, Nenad

Miljkovic and Gang Chen*

*Department of Mechanical Engineering, Massachusetts Institute of Technology, Cambridge, MA,
02139, USA*

* To whom correspondence should be addressed. Email: gchen2@mit.edu

Currently, steam generation using solar energy is based on heating bulk liquid to high temperatures. This approach requires either costly high optical concentrations leading to heat loss by the hot bulk liquid and heated surfaces or vacuum. New solar receiver concepts such as porous volumetric receivers or nanofluids have been proposed to decrease these losses. Here we report development of an approach and corresponding material structure for solar steam generation while maintaining low optical concentration and keeping the bulk liquid at low temperature with no vacuum. We achieve solar-thermal efficiency up to 85% at only 10 kWm^{-2} . This high performance results from four structure characteristics: absorbing in the solar spectrum, thermally insulating, hydrophilic, and interconnected pores. The structure concentrates thermal energy and fluid flow where needed for phase-change and minimizes dissipated energy. This new structure provides a novel approach to harvesting solar energy for a broad range of phase-change applications.

Solar irradiation is a promising source of renewable energy, as the hourly incident solar flux on the surface of the earth is greater than annual global energy consumption¹. Efficient harvesting of solar energy for steam generation is a key factor for a broad range of applications, from large-

scale power generation, absorption chillers, and desalination systems to compact applications such as water purification for drinking, sterilization, and hygiene systems in remote areas where the only abundant energy source is the sun. Current methods of generating steam using solar energy rely on a surface or cavity to absorb the solar radiation, and transferring heat to the bulk liquid directly or via an intermediate carrier fluid, which require high optical concentration and suffer from high optical loss and surface heat loss²⁻⁴, or vacuum to reduce convective heat loss under moderate optical concentration. The steam thus generated is usually in thermal equilibrium with the bulk liquid. Nanofluids---fluids seeded with nanoparticles---as another alternative have been studied⁵⁻⁷ as volumetric absorbers, potentially minimizing the surface energy loss by uniform temperature in the fluid⁶ and enhanced thermal conductivity of nanofluid^{8,9}. Local generation of steam in a cold bulk liquid can be achieved through high concentrations or illumination of nanofluids by electromagnetic waves (generally, lasers) with high power intensity¹⁰⁻¹⁸. Recently, Neumann et al.^{7,19} succeed in generation of steam in bulk water with Au nanoparticles (NPs) with the power of 10^3 kWm^{-2} (optical concentration, C_{opt} , of 1000), consistent with the analysis of Phelan et al.²⁰ on several experiments concluding that Ag NPs with diameter of 20 nm diameter had the lowest threshold light intensity for boiling at $2 \times 10^3 \text{ kWm}^{-2}$. However, the solar-thermal conversion efficiency of the approach was still only 24%. High optical concentrations limit the utilization of these approaches in stand-alone compact solar systems. Furthermore, high optical concentrations add complexity and cost to the solar-thermal conversion system.

We report the development of a new approach and corresponding material structure that localizes the solar energy where evaporation occurs and minimizes the heat losses leading to enhanced solar-thermal efficiency at low optical concentration in open air while generating steam. As

shown in Fig. 1a, under solar illumination, the developed structure forms a hot spot internally where evaporation occurs. The fluid wicks to the hot spot, evaporates and forms vapor which leaves the structure. This structure needs to have four main characteristics: high absorption in the solar spectrum, low thermal conductivity to suppress thermal conduction away from the hot internal region, hydrophilic surfaces to leverage capillary forces and promote fluid flow to the hot region, and interconnected pores for fluid flow to and from the structure.

Results

Material structure. For the first demonstration of this approach, we developed a double layer structure (DLS) consisting of a carbon foam layer supporting an exfoliated graphite layer (Fig. 1b and Fig.1c). The bottom carbon foam is thermally insulating with smaller pore size for liquid supply and the top exfoliated graphite layer has larger pore size for vapor escape. Details of the DLS synthesis are given in the methods section. The optical transmission spectrum of the DLS is measured in the wavelength range of 200-1500 nm (Supplementary Fig. 1a). The reflectivity of the exfoliated graphite is measured with a spectrophotometer equipped with an integrating sphere (Supplementary Fig. 1b) and it is <3 % in the solar spectrum (250-2250 nm). Thus, 97% of the irradiated solar power is absorbed within the top exfoliated graphite layer. The surface area of the exfoliated graphite layer is measured by N₂ adsorption to be approximately 320 m²g⁻¹, 32 times higher than graphite flakes for more efficient heat transfer to the fluid (Supplementary Fig. 2).

Receiver efficiency. Solar absorption in the exfoliated graphite layer generates a hot region in the DLS. If fluid is constantly provided to this hot region, the evaporation rate reaches a steady-state condition. The experimental setup for measurement of evaporation rate (and therefore efficiency) is shown in (Supplementary Fig. 3). A test chamber is designed to assess

performance of the DLS. This design is aimed to minimize 2-D and 3-D thermal losses. The thermal losses by the test chamber is simulated and discussed in (Supplementary Fig. 4). The lab-scale size of the test chamber leads to a total of 6.5% parasitic losses, which can be avoided in large scales applications (Supplementary Note 4). Hence, higher receiver efficiency can be achieved in large systems. The evaporation rates of water with the DLS and the single exfoliated graphite layer (volumetric absorber) are measured by recording the weight change as a function of time and results are compared with pure water under solar illumination of 1 and 10 kWm^{-2} , Fig. 2a and 2b. After an initial transient period, the evaporation rate reaches a constant value. At each optical concentration, an experiment was run for a long illumination time (more than 5 hours) and no change in evaporation rate is observed after the initial transient period. For pure water, the absorptance is small in the visible range. However, this small absorptance together with the larger absorptance in the infrared regime (not directly measured in this work) throughout the volume of the water causes an approximately 10 °C temperature rise in steady state condition under a solar intensity of 1 kWm^{-2} . This temperature rise leads to enhanced evaporation (~6 times) compared to a dark environment (Supplementary Fig. 5). The water evaporation rate in a dark environment is 74 $\text{kgm}^{-2}\text{hr}^{-1}$. This “dark” evaporation rate is subtracted from all the measured evaporation rates under the solar illumination to isolate the effect of solar irradiation on the evaporation rate. The DLS structure shows the highest evaporation rate and it is 2.1 and 2.4 times higher than pure water at 1 and 10 kWm^{-2} solar illumination, respectively. To show the effect of the bottom layer of the DLS, if only exfoliated graphite (volumetric absorber) is utilized, the evaporation rate drops by 17% due to heat losses by conduction to the underlying water. The thermal efficiency (η_{th}) is considered to assess the performance of DLS and is defined as

$$\eta_{\text{th}} = \frac{\dot{m} h_{\text{LV}}}{C_{\text{opt}} q_i} \quad (1)$$

where \dot{m} denotes the mass flux, h_{LV} total enthalpy of liquid-vapor phase change (sensible heat+ phase-change enthalpy), C_{opt} the optical concentration, and q_i the nominal direct solar irradiation 1 kWm^{-2} . The η_{th} of the DLS is an increasing function of optical concentration and goes from 64% at 1 kWm^{-2} to 85 % at 10 kWm^{-2} , Fig. 2c. We emphasize that optical concentration losses are not considered in this analysis. Note that this level of optical concentration can be achieved by simple non-imaging optics with monthly adjustment without a tracking system, which reduce the overall cost of the system. We calculate the conduction losses to the underlying water as described in (Supplementary Fig. 6 and Supplementary Fig. 7). This loss at 10 kWm^{-2} is $5 \pm 0.5 \%$ of the total solar irradiation. The measured surface temperature of the exfoliated graphite is ~ 5 °C less than the generated vapor temperature. Considering emissivity of 0.97 (Supplementary Fig. 1b), under solar illumination of 10 kWm^{-2} , the radiation losses at the surface are 6 %. At a solar irradiation of 1 kWm^{-2} , the fraction of losses is $\sim 35\%$ (reflection $\sim 3\%$, conduction $\sim 6\%$, surface radiation $\sim 12\%$, test chamber parasitic losses $\sim 14\%$). These losses are a decreasing function of solar irradiation, and the total loss drops to $\sim 15\%$ at 10 kW^{-2} . If the steam is generated with the DLS at higher concentrations, we expect that efficiencies of more than 90 % is achievable. Here, we focused on low optical concentration to reduce the complexity and cost of solar harvesting system.

As a comparison, we have prepared a highly absorbing nanofluid with carbon black NPs. The structures of NPs are shown in (Supplementary Fig. 8). The sample preparation method is given in (Supplementary Note 7). The nanofluid has absorption of $> 99\%$ in the wavelength range of 250-2250 nm. We have measured the receiver efficiency of this absorber with the same procedure used for the DLS (Supplementary Fig. 9a). The vapor generation rate by this type of

receiver at solar irradiation of 10 kWm^{-2} is compared with the DLS in (Supplementary Fig. 9b). The nanofluid receiver leads to both lower vapor temperature ($\sim 80 \text{ }^\circ\text{C}$) and lower efficiency compared to the DLS. The conversion efficiency of nanofluid receiver at solar irradiation of 10 kWm^{-2} is $75\pm 3\%$ while this efficiency for the DLS is $85\pm 3\%$. Furthermore, the fast dynamics of steam generation by the DLS is caused by heat localization at the liquid-vapor interface making it a superior option in transient solar irradiation applications.

The evaporation rate as a function of optical concentrations is also shown in Fig. 2c. Localized energy close to the surface of the structure accompanied by a limited flow rate of fluid leads to an enhanced temperature of the generated vapor phase. At 10 kWm^{-2} , while steam is generated, the underlying liquid is close to ambient temperature as shown in Fig. 2d. This non-equilibrium process offers a localized phase-change while the surrounding medium remains cold. This localization leads to a significant drop in thermal losses by the bulk fluid and consequently a boost in the thermal efficiency of solar-thermal conversion. Note that our current system does not allow us to conduct experiments at higher pressures.

Structure characterization. Low thermal conductivities of the materials in the DSL structures are important for heat localization. We measured the thermal conductivity of each layer in this structure separately. The thermal conductivity of each layer is measured with an IR microscope (See details in methods). In Figs. 3(a-d), the thermal conductivity of each layer in air (Fig. 3a and 3b) and filled with water (Fig. 3c and 3d) are shown. The inset in each figure is a representative picture taken by IR microscope and indicates the temperature gradient across the sample. Since both structures are porous and have a large portion of air, their thermal conductivity is low in air. Once the exfoliated graphite (top layer) is filled with water, its thermal conductivity is larger than that of water and is not favorable for localizing heat, see Fig. 3c.

However, the carbon foam shows a low thermal conductivity even when soaked in water. The carbon foam (bottom layer of the DLS) is critical for localizing thermal energy and the low thermal conductivity is due to the closed pores in this structure. These closed pores have three advantages: floating the structure, lowering the thermal conductivity, and limiting the fluid flow to the surface. Low thermal conductivity and limited fluid flow lead to formation of a hot spot and generation of steam in the DLS at low optical concentrations. In contrast to closed pores, open pores provide paths for fluid to flow to the surface.

The other important characteristic of the DLS is its hydrophilicity which promotes fluid flow to the surface. The capillary force in the exfoliated graphite layer enhances the evaporation rate of the fluid through several mechanisms: formation of thin films on the surface of graphite sheets²¹, enhanced surface area for evaporation²², and formation of three-phase contact lines at the edges of the capillaries^{23,24}. The graphite structure has hydrophobic surfaces as evidenced by the contact angle (Supplementary Fig. 10a). However, after exfoliation in a microwave and oxidization of its surface, the graphite surface becomes hydrophilic (Supplementary Fig. 10b). The microstructure of graphite flakes before and after microwave exfoliation is presented in (Supplementary Fig. 11). In practice, while the hydrophobic graphite flake appears dry on the water surface (see Fig. 4a), the hydrophilic graphite flake results in formation of a thin layer of water on the top surface (see Fig. 4b). The hydrophilic flakes leverage the capillary force to channel the fluid flow to the hot region. The microstructure of carbon foam is shown in (Supplementary Fig. 12a). The pores diameters are around 300-600 μm . Furthermore, the role of closed pores in floating the structure is highlighted in (Supplementary Fig. 12b) by comparing it with a carbon foam consisting of only open pores. In Fig. 4c, powdered carbon foam is dispersed on a water surface forming a dry surface indicating the hydrophobicity of this foam. To promote

water flow, the carbon foam is treated by 4% molar nitric acid (see methods section), to make its surface hydrophilic, Fig. 4d.

Efficiency comparison. To illustrate the insulating role of carbon foam, the underlying liquid temperature under the solar illumination of 1 kWm^{-2} is measured for the DLS experiments and compared to just exfoliated graphite and pure water cases, as shown in Fig. 5a. Note that the thermocouples are shielded to eliminate the effect of direct solar illumination in the pure water experiments. As shown, the temperature of the water 15 mm below the water surface with the DLS structure is half of that in the other cases. In the absence of the bottom insulating foam, the temperature exceeds that of the pure water case due to a hot spot created in the exfoliated graphite layer. The generated vapor temperature with the DLS is measured under a range of optical concentrations and is plotted in Fig. 5b. With the DLS, steam $>100 \text{ }^\circ\text{C}$ is generated at the solar illumination of 10 kWm^{-2} . A few degrees higher steam temperature than saturation temperature at the ambient pressure is caused by the superheat required for heterogeneous bubble nucleation. Based on the measured vapor temperature and evaporation mass flux, receiver efficiency of the DLS is determined for 1, 2 and 10 kWm^{-2} solar irradiation, Fig. 5c. At each solar concentration, this efficiency is compared with the receiver efficiency of water and single graphite layer on water. As shown, the DLS offers a high performance in solar-thermal energy conversion compared to both cases.

Furthermore, the performance of the DLS is compared with some reported state-of-the-art systems²⁵ (selective absorbers, nanofluids, and a type of volumetric absorber) and is presented in Fig. 5d. Note that all the systems are non-vacuum and no optical concentration losses are considered. These intrinsic efficiencies are plotted as a function of $(T_{\text{max}}-T_{\text{am}})/C_{\text{opt}}$ where T_{max} denotes maximum temperature of working fluid in the receiver and T_{am} the ambient temperature

(Supplementary Note 7). As shown, DLS offers better performance than reported values of these systems and promises a new efficient approach for solar-thermal harvesting. In addition, in the (Supplementary Note 10) potential applications of the DLS are presented.

In conclusion, we have developed an approach and corresponding material structure, the DLS, which absorbs solar illumination, and confines the thermal energy (formation of hot spot) to near the structure surface while efficiently wicking the fluid to this hot spot. This structure yields a solar-thermal conversion efficiency of 85% at 10 kWm^{-2} solar illumination, while generating steam in open air. Localization of heat is achieved by the broad-spectrum absorbing and thermally insulating properties of the DLS while the fluid flow is channeled to the hot spot by the hydrophilic and porous nature of the DLS. We believe that by decreasing the flow rate in the carbon foam, replacing carbon foam with a more insulating material, and optimizing porosity and thickness of each layer (tuning capillary pressure in the structure) better performance such as higher steam temperature and/or at lower optical concentrations can be achieved. This work opens a new approach for solar assisted steam generation for many potential applications.

Methods

Synthesis of the DLS. The acid-washed graphite flakes are obtained from Anthracite Industries Inc. The acid-washed graphite flakes are mixed with the iron (II) acetate anhydrous, 97% (Strem Chemicals) with the ratio of 60-40 wt%. The mixture was heated in a microwave for 7s to form an exfoliated fluffy structure²⁶⁻²⁸. The trapped gases between the graphite layers expand in the synthesis process and detach the flakes from each other. The volumetric exfoliation during this process is approximately 100 times. The dispersed iron species formed after the decomposition of Iron (II) acetate provides a ferromagnetic structure. The ferromagnetism of the exfoliated graphite helps its collection after use. The acid-washed graphite flakes originally have a hydrophobic

surface. However, in the exfoliation process, due to high temperature, the graphite surface is oxidized and turns into a hydrophilic surface. The Duocel carbon foam of type PPI 80 (80 pores per inch) is purchased from K. R. Reynolds. The carbon foam is washed in 4% molar nitric acid for 2 hrs under stirring to make its surface hydrophilic.

Thermal conductivity measurements by IR microscope. The thermal conductivity of each material is measured by sandwiching the material between two squared-shape glass slabs (reference materials) each 1 mm thick. The glass slabs are spaced from each other by double-stick tape and sealed in three sides for liquid measurements. The sandwich is placed between a heat source (Cu block heater) and a heat sink (thermoelectric cooler). The heat sink is maintained at a fixed temperature while the current through the heat source is tuned to induce a range of temperature gradients across the sandwich. The whole structure is placed under an IR microscope. The emissivity map of the sandwich in an isothermal condition is first obtained followed by temperature distribution mapping. Since the thermal conductivity of reference materials is known, the measured temperature gradient in these materials is used to determine the heat flux. Given the heat flux, and measured temperature gradient in the material, the thermal conductivity of each material is calculated by the Fourier equation. The set-up is calibrated with water first and the measured thermal conductivity is within $\pm 5\%$ of the reported value. The linear correlation of heat flux and temperature gradient in Fig. 3 suggests a negligible contribution of convection side losses in the measurements.

References

1. Lewis, N. S. Toward cost-effective solar energy use. *Science* **315**, 798–801 (2007).

2. Lenert, A. & Wang, E. N. Optimization of nanofluid volumetric receivers for solar thermal energy conversion. *Sol. Energy* **86**, 253–265 (2012).
3. Fend, T., Hoffschmidt, B., Pitz-Paal, R., Reutter, O. & Rietbrock, P. Porous materials as open volumetric solar receivers: Experimental determination of thermophysical and heat transfer properties. *Energy* **29**, 823–833 (2004).
4. Kribus, A., Doron, P., Rubin, R. & Karni, J. A Multistage Solar Receiver:: The Route To High Temperature. *Sol. Energy* **67**, 3–11 (1999).
5. Tyagi, H., Phelan, P. & Prasher, R. Predicted Efficiency of a Low-Temperature Nanofluid-Based Direct Absorption Solar Collector. *J. Sol. Energy Eng.* **131**, 041004 (2009).
6. Otanicar, T. P., Phelan, P. E., Prasher, R. S., Rosengarten, G. & Taylor, R. a. Nanofluid-based direct absorption solar collector. *J. Renew. Sustain. Energy* **2**, 033102 (2010).
7. Neumann, O. *et al.* Solar Vapor Generation Enabled by Nanoparticles. *ACS Nano* **7**, 42–9 (2012).
8. Wang, X.-Q. & Mujumdar, A. S. Heat transfer characteristics of nanofluids: a review. *Int. J. Therm. Sci.* **46**, 1–19 (2007).
9. Eastman, J. a., Choi, S. U. S., Li, S., Yu, W. & Thompson, L. J. Anomalously increased effective thermal conductivities of ethylene glycol-based nanofluids containing copper nanoparticles. *Appl. Phys. Lett.* **78**, 718 (2001).
10. Govorov, A. O. & Richardson, H. H. Generating heat with metal nanoparticles. *Nano Today* **2**, 30–38 (2007).
11. Govorov, A. O. *et al.* Gold nanoparticle ensembles as heaters and actuators: melting and collective plasmon resonances. *Nanoscale Res. Lett.* **1**, 84–90 (2006).
12. Richardson, H. H. *et al.* Thermo-optical Properties of Gold Nanoparticles Embedded in Ice: Characterization of Heat Generation and Melting. *Nano Lett.* **6**, 783–788 (2006).
13. Ekici, O. *et al.* Thermal Analysis of Gold Nanorods Heated with Femtosecond Laser Pulses. *J. Phys. D. Appl. Phys.* **41**, 185501 (2008).
14. Kotaidis, V., Dahmen, C., von Plessen, G., Springer, F. & Plech, a. Excitation of nanoscale vapor bubbles at the surface of gold nanoparticles in water. *J. Chem. Phys.* **124**, 184702 (2006).
15. Lapotko, D. Optical excitation and detection of vapor bubbles around plasmonic nanoparticles. *Opt. Express* **17**, 2538–56 (2009).

16. Schmidt, A. J. *et al.* Probing the Gold Nanorod–Ligand–Solvent Interface by Plasmonic Absorption and Thermal Decay. *J. Phys. Chem. C* **112**, 13320–13323 (2008).
17. Sershen, S. R., Westcott, S. L., Halas, N. J. & West, J. L. Temperature-sensitive polymer – nanoshell composites for photothermally modulated drug delivery. *J. Biomed. Mater. Res.* **51**, 293–298 (2000).
18. Jones, C. D. & Lyon, L. A. Photothermal patterning of microgel/gold nanoparticle composite colloidal crystals. *J. Am. Chem. Soc.* **125**, 460–5 (2003).
19. Neumann, O. *et al.* Compact solar autoclave based on steam generation using broadband light-harvesting nanoparticles. *Proc. Natl. Acad. Sci. U. S. A.* **110**, 11677–81 (2013).
20. Phelan, P., Taylor, R., Adrian, R., Prasher, R. & Otanicar, T. in *Nanoparticle Heat Transf. Fluid Flow* (Minkowycz, W. J., Sparrow, E. M. & Abraham, J.) 123–142 (CRC Press, 2012).
21. Zhang, W., Shen, R., Lu, K., Ji, A. & Cao, Z. Nanoparticle enhanced evaporation of liquids: A case study of silicone oil and water. *AIP Adv.* **2**, 042119 (2012).
22. Kim, H. & Kim, J. Evaporation characteristics of a hydrophilic surface with micro-scale and/or nano-scale structures fabricated by sandblasting and aluminum anodization. *J. Micromechanics Microengineering* **20**, 045008 (2010).
23. Ghasemi, H. & Ward, C. A. Energy transport by thermocapillary convection during Sessile-Water-droplet evaporation. *Phys. Rev. Lett.* **105**, 136102 (2010).
24. Deegan, R. D. *et al.* Capillary flow as the cause of ring stains from dried liquid drops. *Nature* **389**, 827–829 (1997).
25. Taylor, R. a. *et al.* Applicability of nanofluids in high flux solar collectors. *J. Renew. Sustain. Energy* **3**, 023104 (2011).
26. Zheng, R., Gao, J., Wang, J. & Chen, G. Reversible temperature regulation of electrical and thermal conductivity using liquid-solid phase transitions. *Nat. Commun.* **2**, 289 (2011).
27. Zheng, R. *et al.* Thermal Percolation in Stable Graphite Suspensions. *Nano Lett.* **12**, 188–192 (2012).
28. J. Vivas-Castro, G. Rueda-Morales, G. Ortega-Cervantez, J. Ortiz-López, L. M.-R. and M. O.-A. in *Carbon Nanotub. - Synth. Charact. Appl.* (Yellampalli, S.) 47–60 (InTech, 2011).

Acknowledgements

We would like to thank Jianjian (James) Wang, Xiansen Li, and Kenneth McEnaney for their assistance in the experiments. This work is support mainly by ‘Solid State Solar-Thermal Energy Conversion Center (S³TEC), an Energy Frontier Research Center funded by the US Department of Energy, Office of Science, Office of Basic Energy Sciences under Award Number: DE-SC0001299/DE-FG02-09ER46577 (H.G. for solar thermal basic science), by AFOSR FA9550-11-1-0174 (A.M. for graphite synthesis), and by MASDAR (G.N., for potential power plant applications). Hadi Ghasemi thanks Natural Sciences and Engineering Research Council of Canada (NSERC) for their support.

Author Contributions

H.G. and A.M. developed the concept. H.G., G.N., A.M., J.L., S.Y., N. M designed and executed the experiments and analyzed the data. H. G. wrote the manuscript and all of the authors commented on the manuscript. G.C. directed the research.

Competing Financial Interests

The authors declare no competing financial interests. MIT has applied for a patent, application No. 61/874390 related to the design and application of this material structure. Supplementary Information accompanies this paper online. Correspondence should be addressed to G.C. (gchen2@mit.edu)

Figure legends

Figure 1 | Double layer structure (a) A representative structure for localization of heat; the cross section of structure and temperature distribution (b) The DLS that consists of a carbon foam (10 mm thick) supporting an exfoliated graphite layer (~5 mm thick). Both layers are hydrophilic to promote the capillary rise of water to the surface (c) A picture of enhanced steam generation by the DLS structure under the solar illumination of 10 kWm^{-2} .

Figure 2 | Performance of the double layer structure The evaporation mass loss of water with different structures under (a) 1 kWm^{-2} and (b) 10 kWm^{-2} solar irradiation is compared with the case of pure water. All experiments are conducted in ambient temperature of $24 \text{ }^\circ\text{C}$ and the humidity of 31%. (c) The solar-thermal efficiency of the evaporation process by the DLS under a range of optical concentrations (left-hand side axis) and the corresponding evaporation rate (right-hand side axis). (d) While the steam is generated, the underlying bulk liquid is at the ambient temperature.

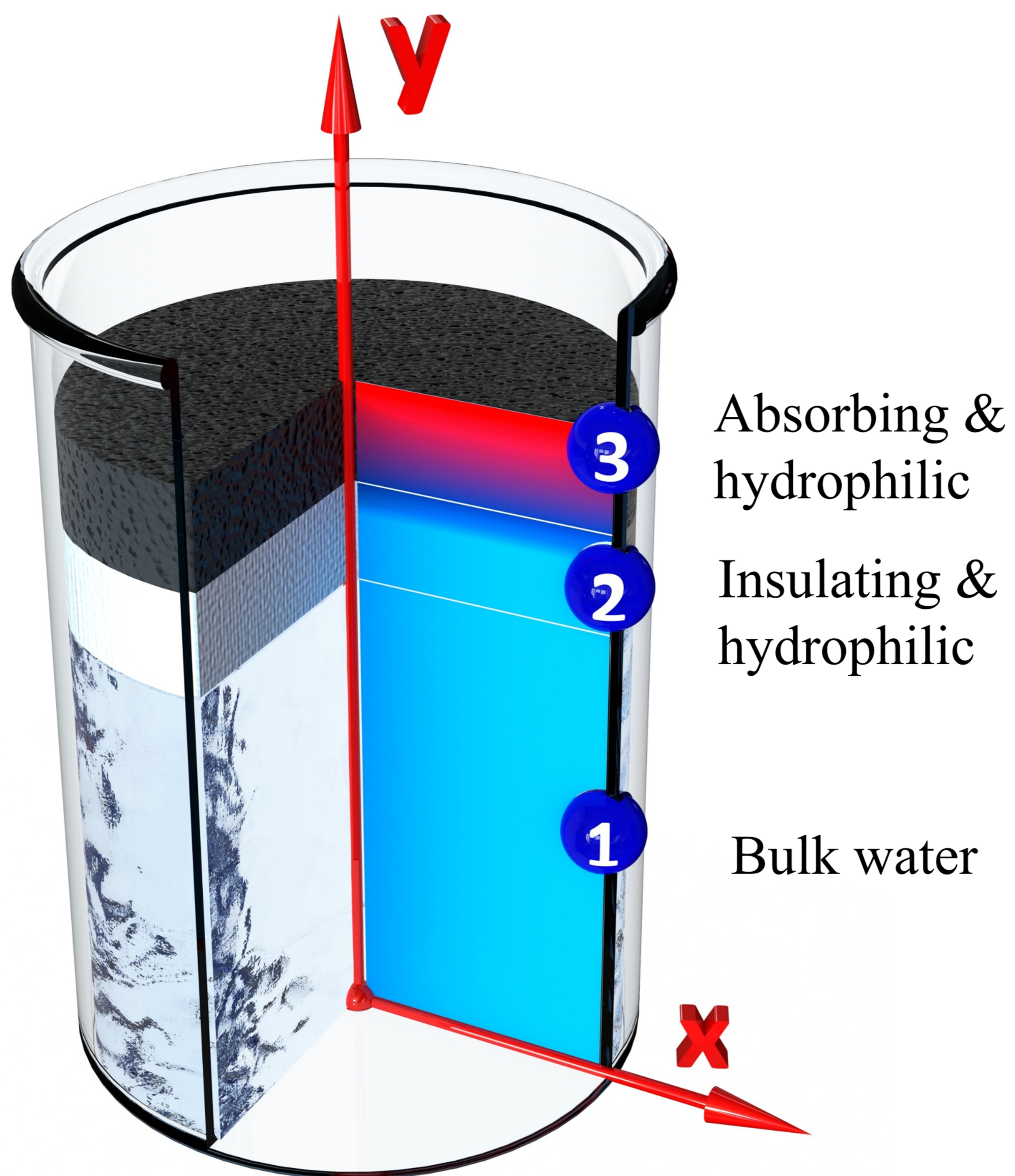
Figure 3 | Thermal conductivity of the double layer structure The thermal conductivity of each layer in the DLS is measured by an IR microscope (methods). (a) Exfoliated graphite in air, (b) carbon foam in air, (c) exfoliated graphite with water, and (d) carbon foam filled with water. The inset in the figures are the representative picture taken by IR microscope.

Figure 4 | Hydrophilicity of the double layer structure (a) The as-purchased graphite flakes possess hydrophobic surfaces and form a blanket over the water surface (b) The synthesized graphite flakes are hydrophilic and form a thin layer of water on the surface (c) The powdered

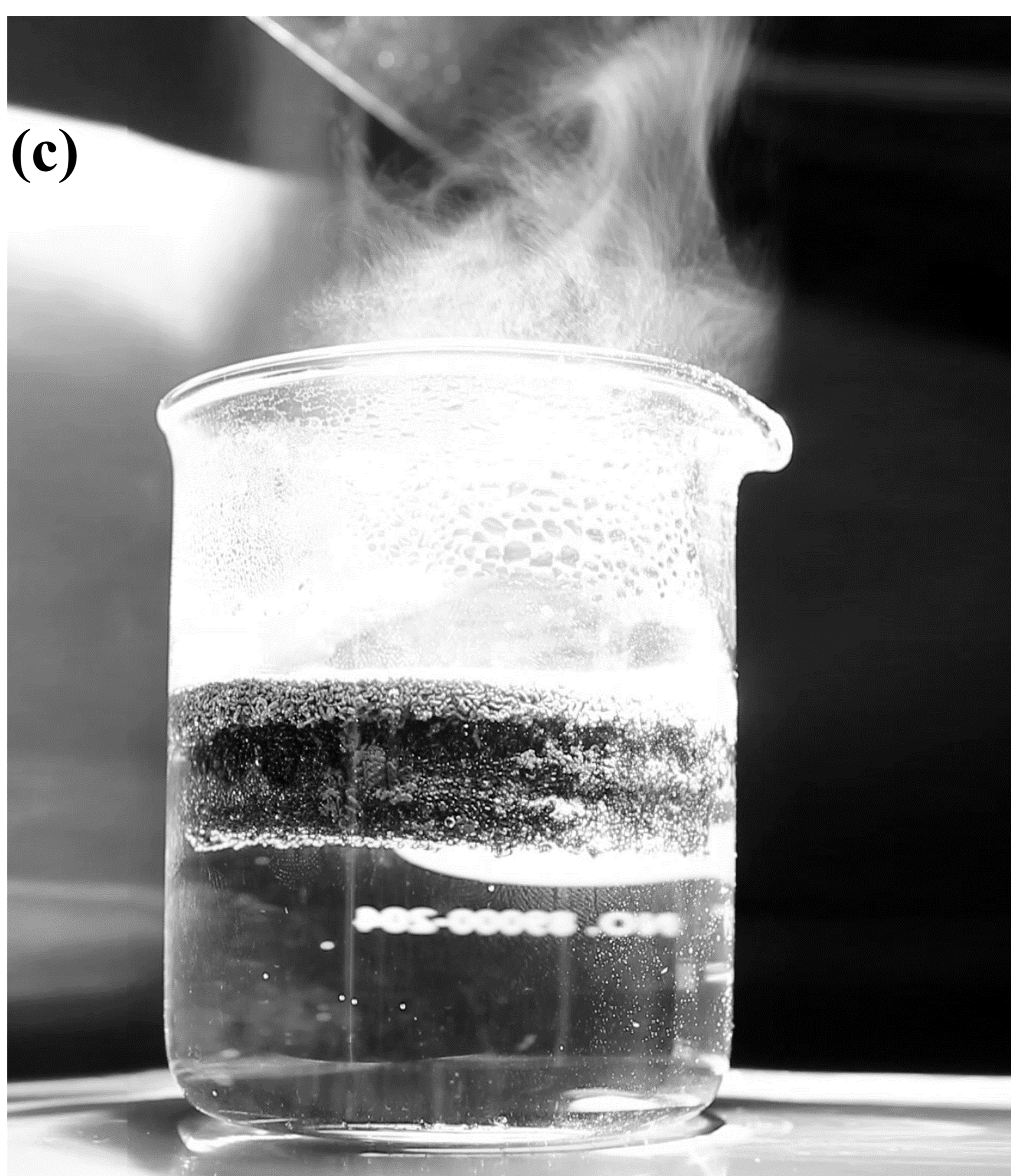
carbon foam which is hydrophobic (d) The processed carbon foam which is hydrophilic and promotes the capillary force and infiltration of water to the surface.

Figure 5 | Efficiency comparison (a) The insulating behavior of carbon foam is highlighted by measurement of underlying water temperature under 1 kWm^{-2} and compared with other structures. For pure water, a radiation shield was installed on top of the thermocouple to eliminate the effect of direct radiation on the temperature reading. For the carbon structures, the transmittance of the structure is low enough that direct radiation does not contribute in temperature measurements. (b) The generated vapor temperature with the DLS under a range of optical concentrations (c) The solar-thermal conversion efficiency of the DLS is compared with water and single graphite layer under 1, 2, 10 kWm^{-2} solar illumination. Furthermore, the receiver efficiency of a highly absorbing nanofluid is shown. The error bars in the efficiency values resulted from errors in the measurement of solar irradiation power and evaporation flux and the error bars in the evaporation flux are resulted from error in the mass change measurements. (d) The performance of DLS is compared with the current systems as a receiver in a solar tower collector²⁵. All of these systems are non-vacuum and no optical concentration losses are considered in these data.

(a)



(c)



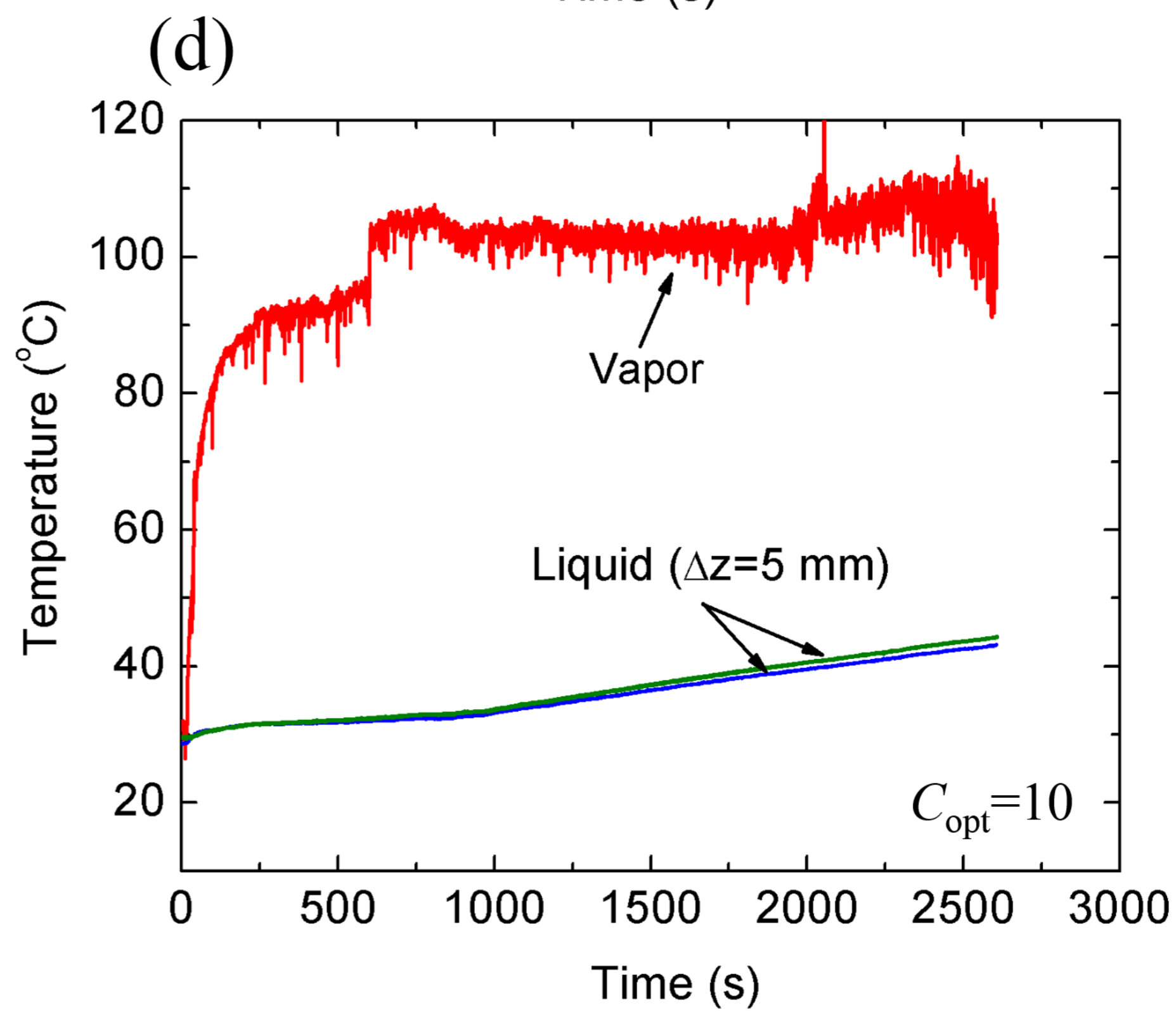
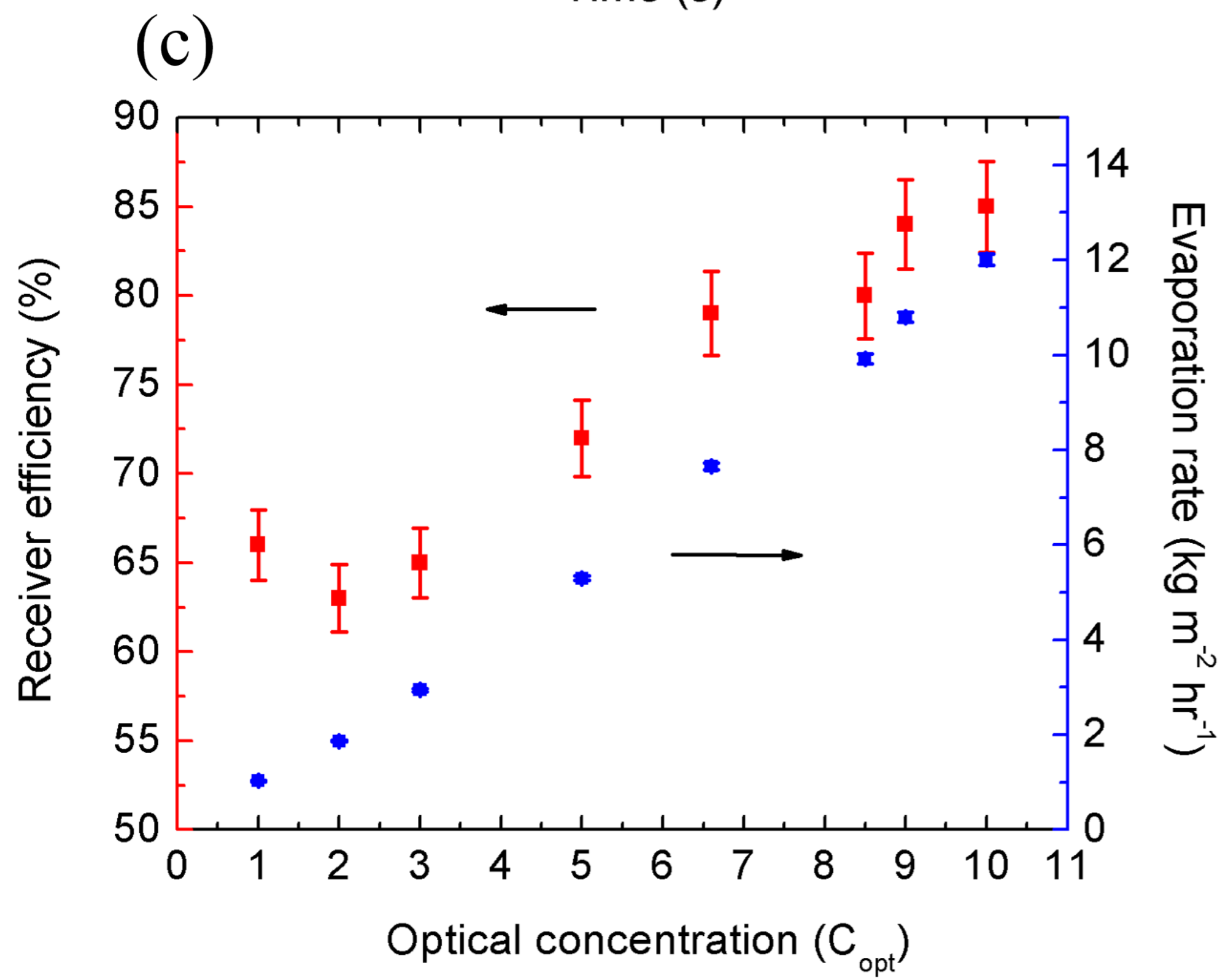
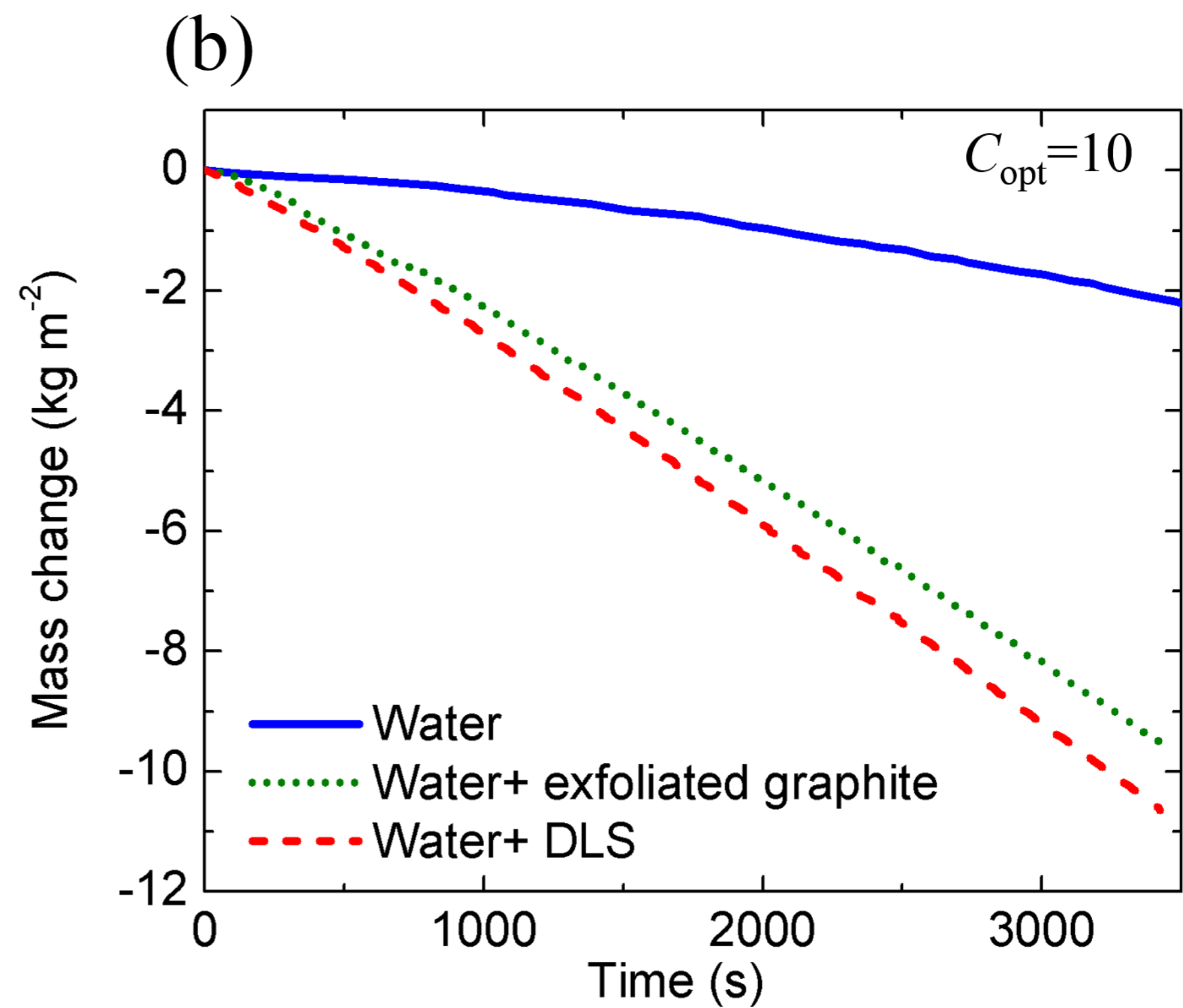
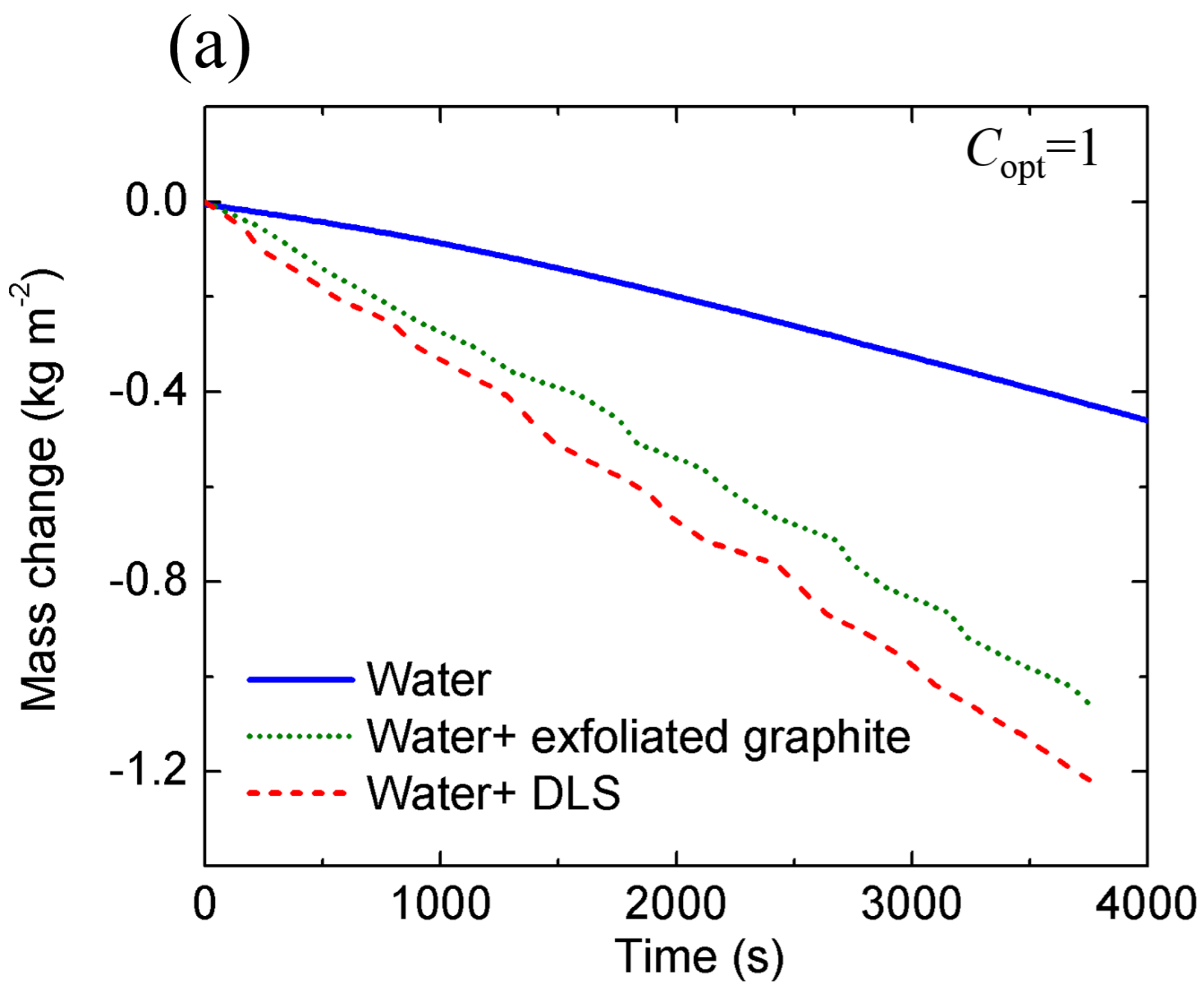
(b)

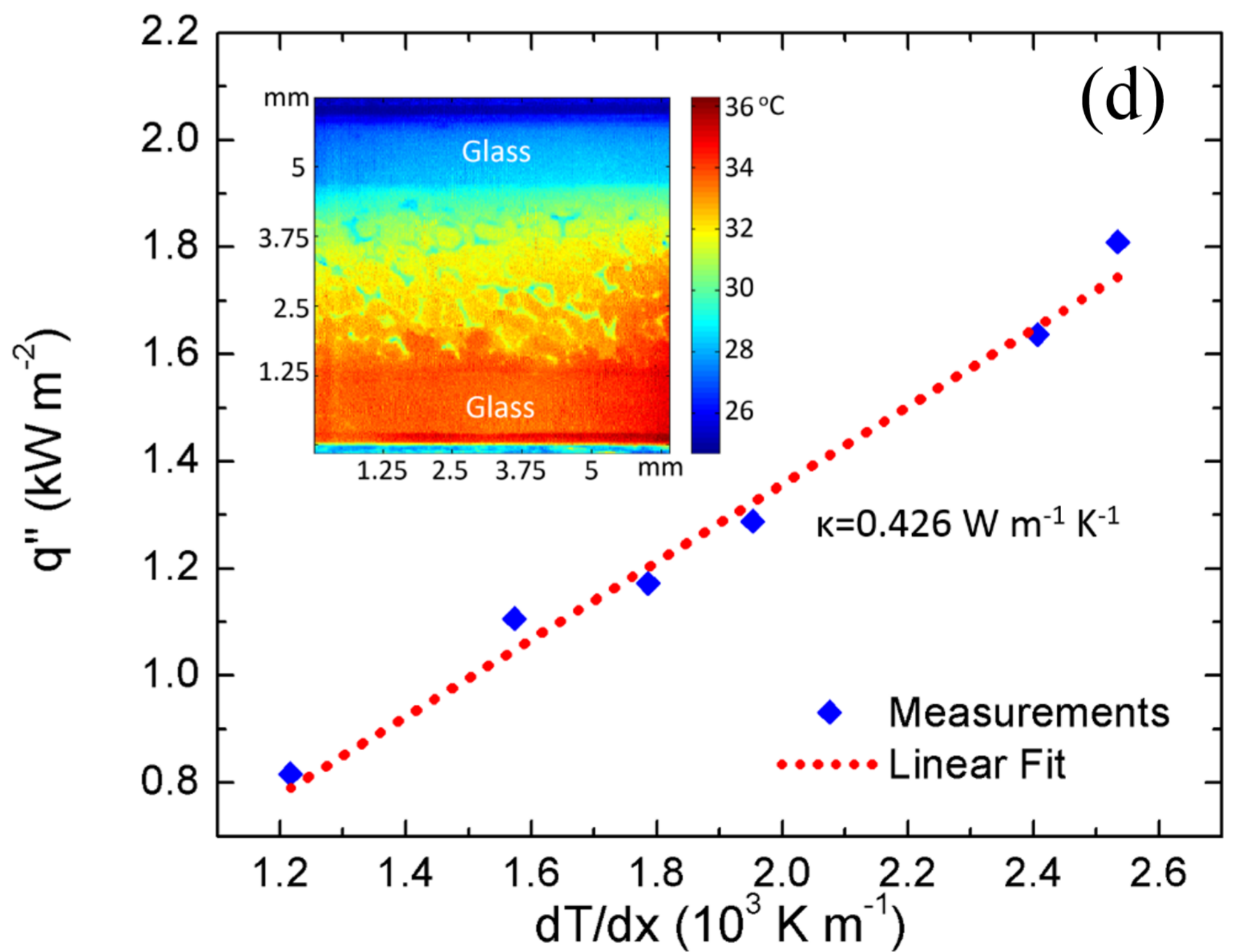
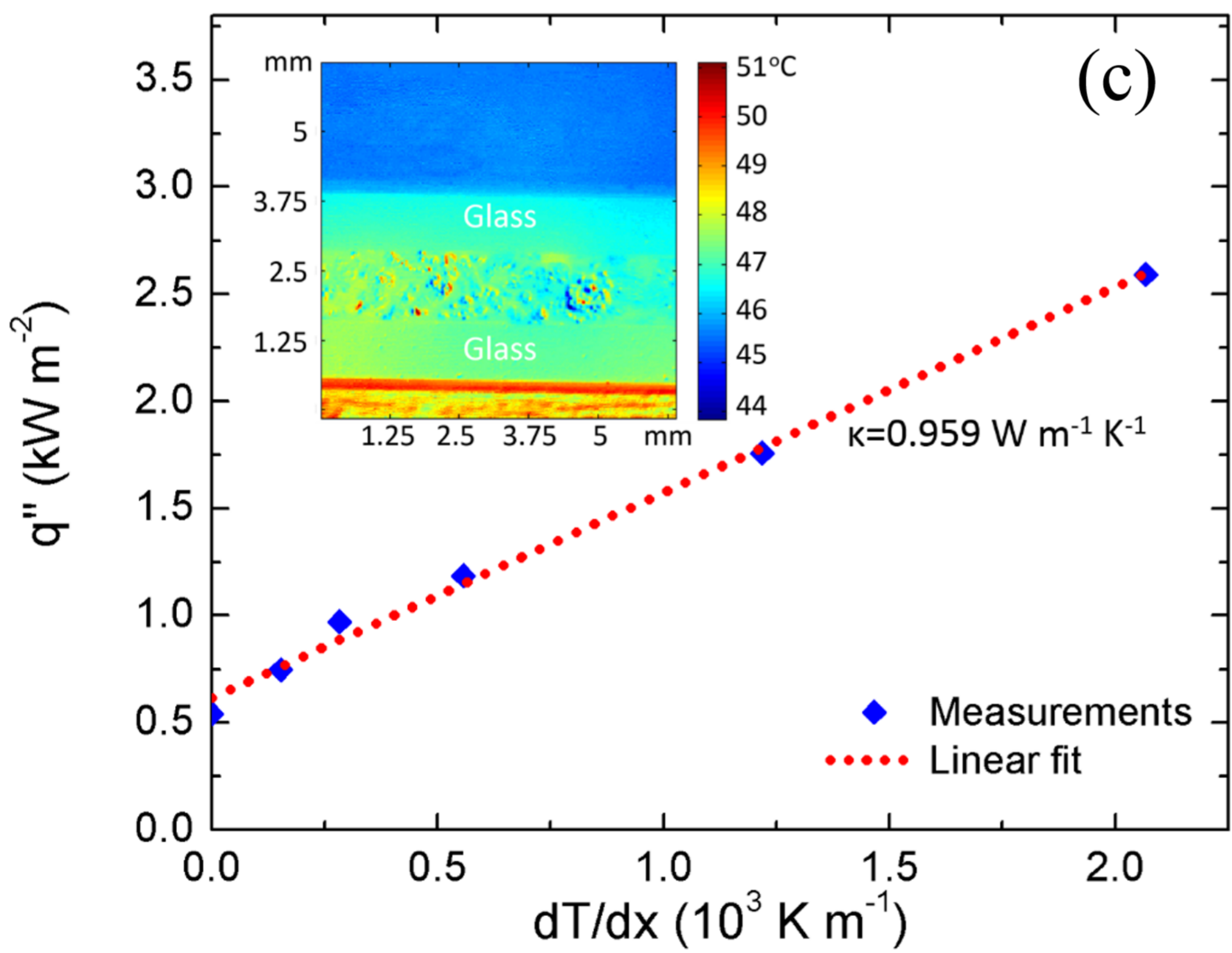
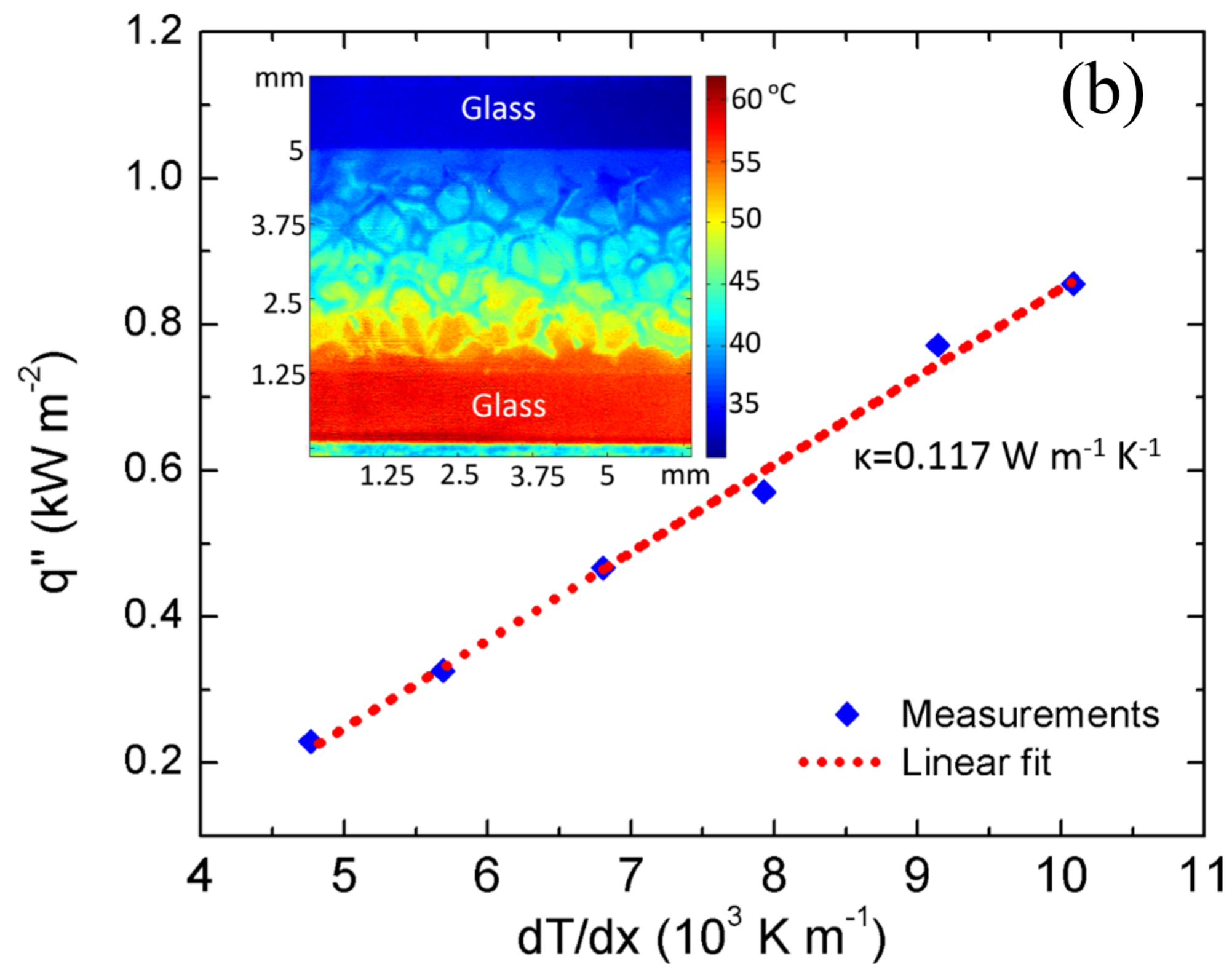
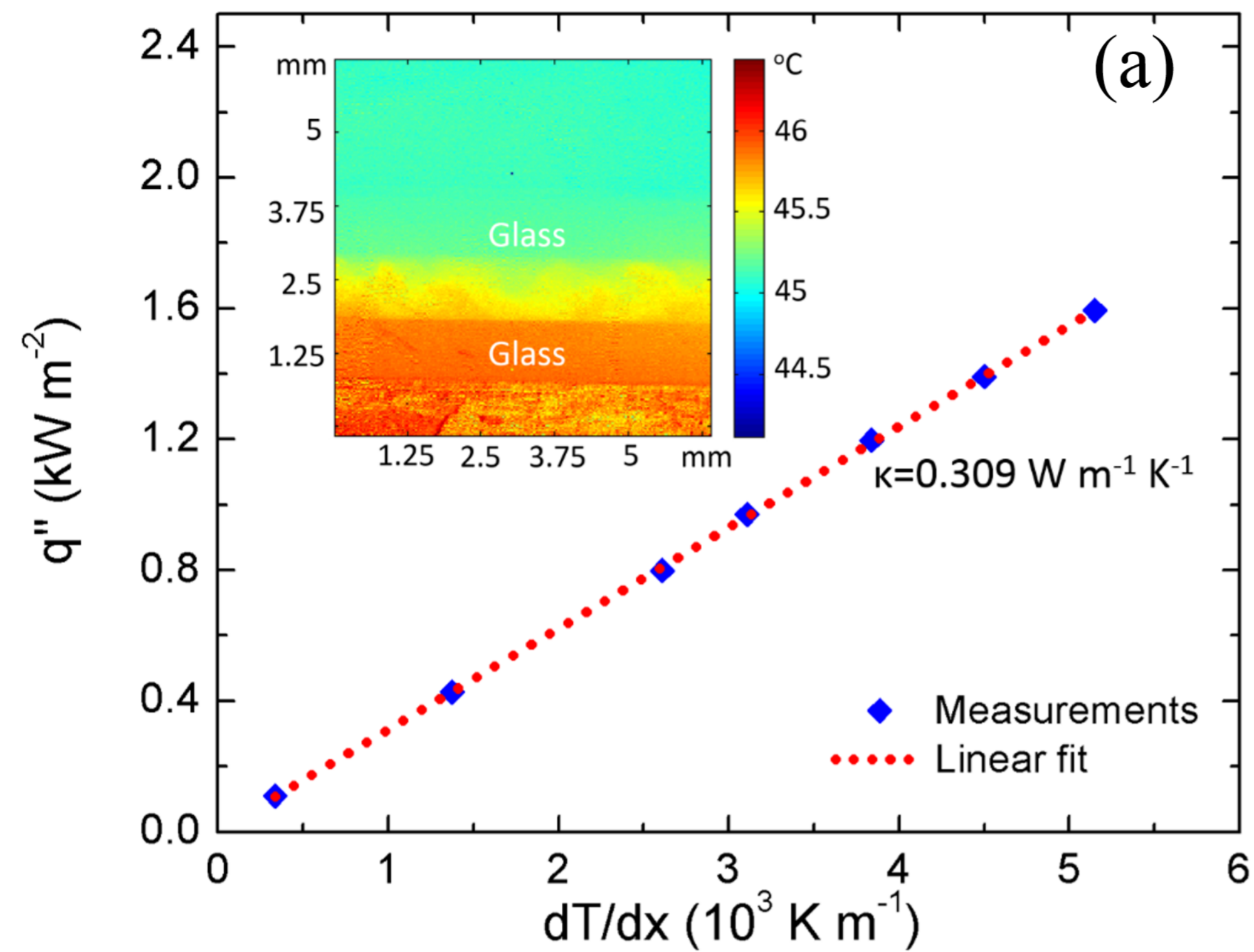
Representative structure for heat localization

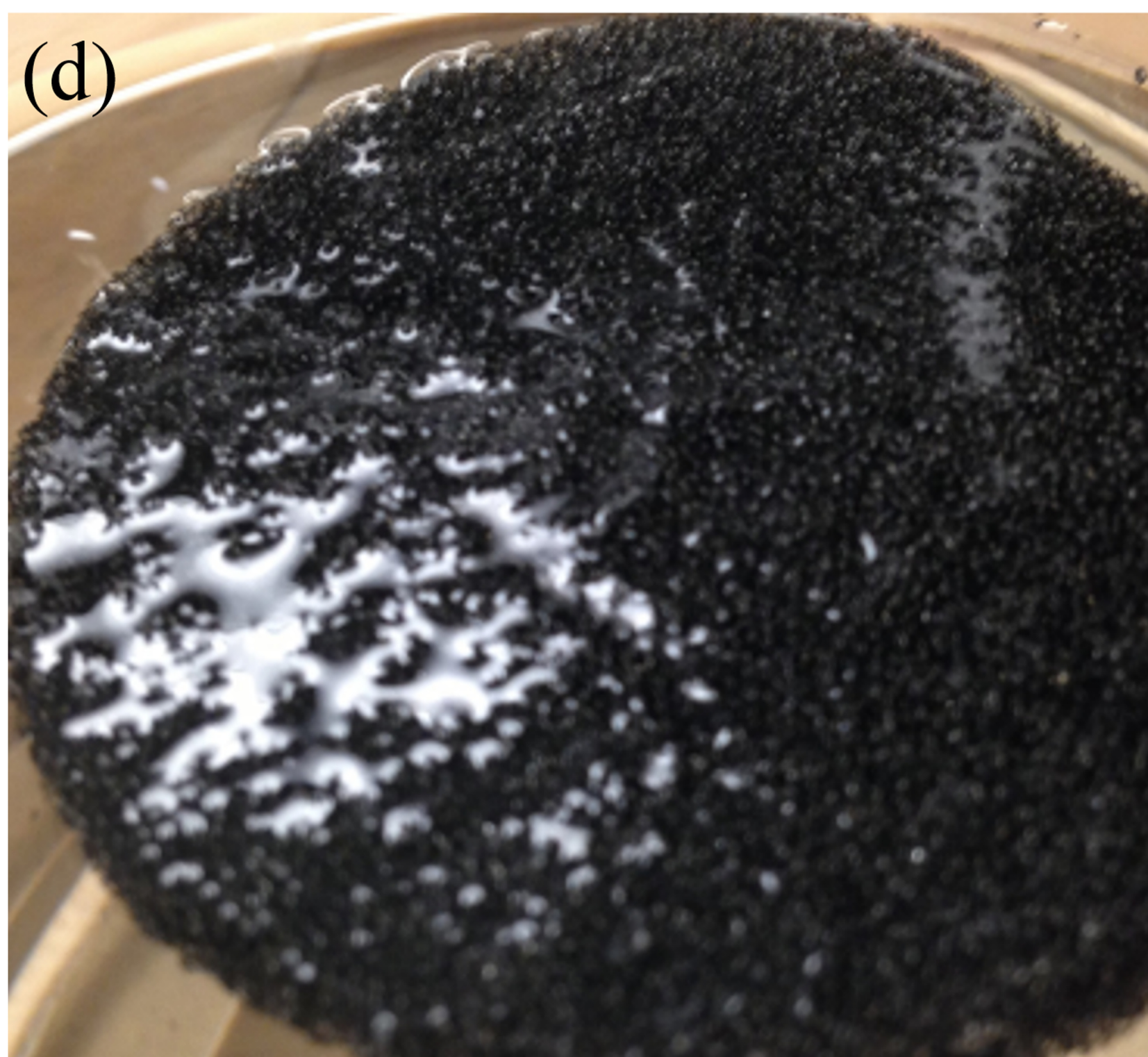
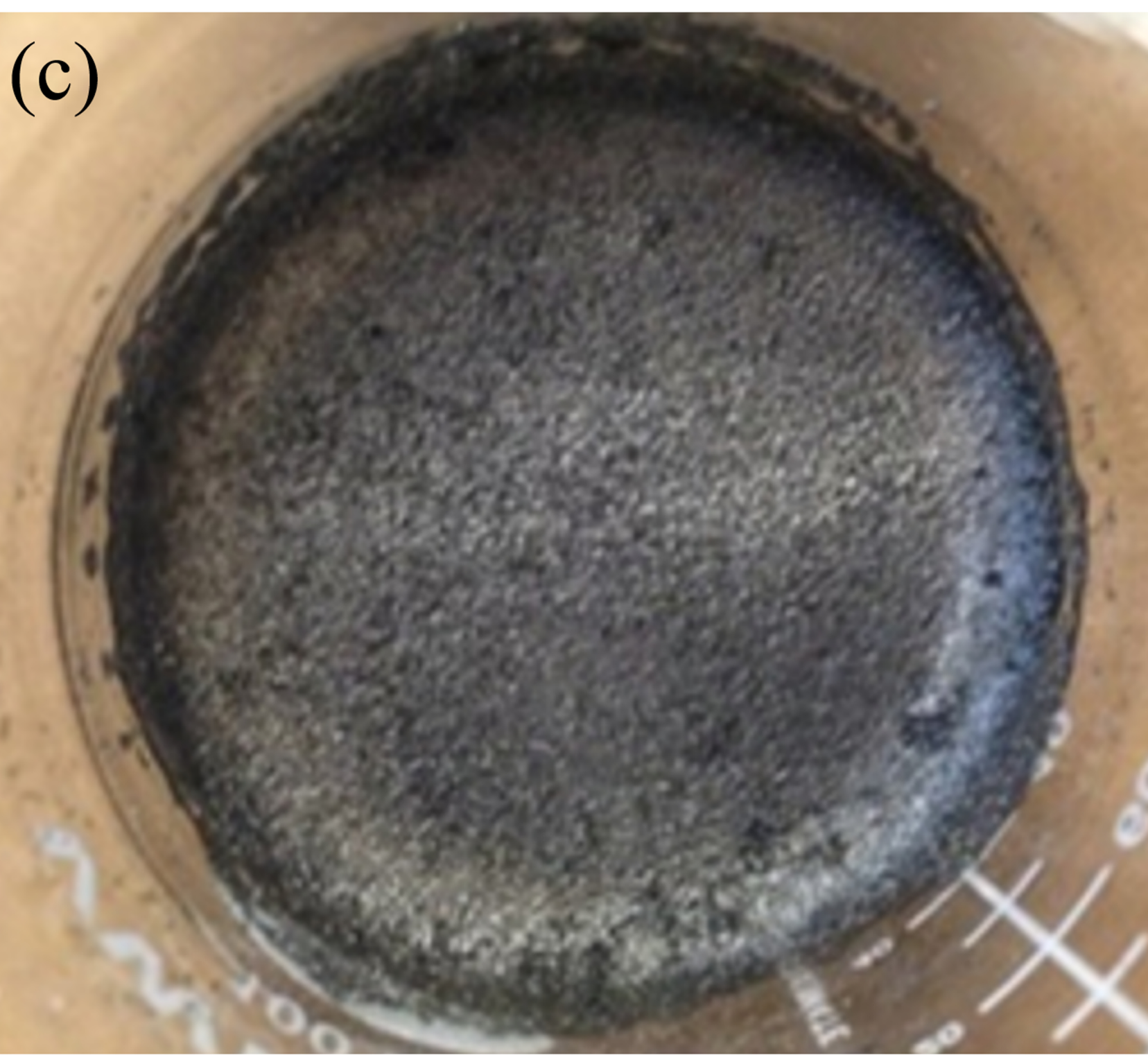
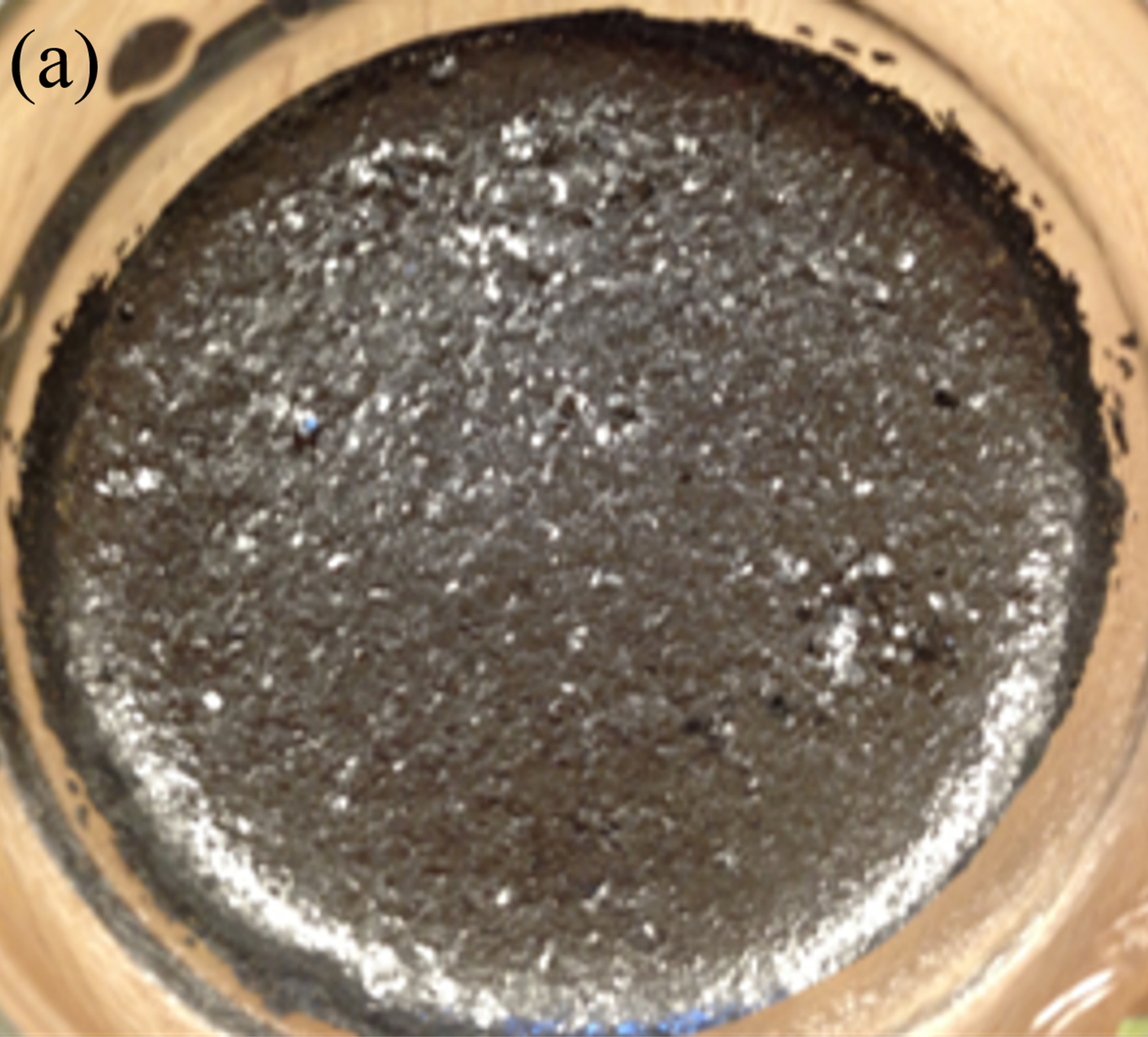


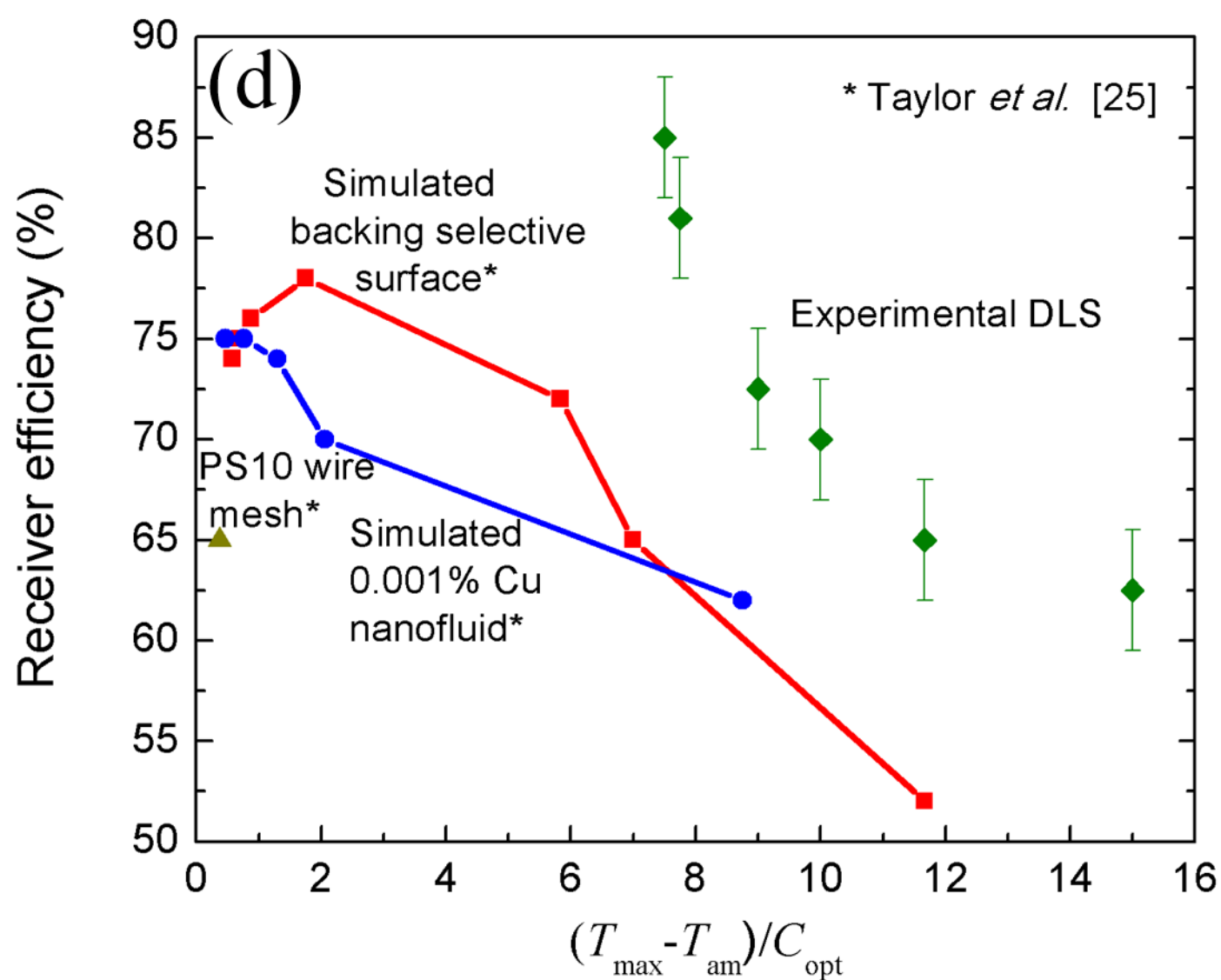
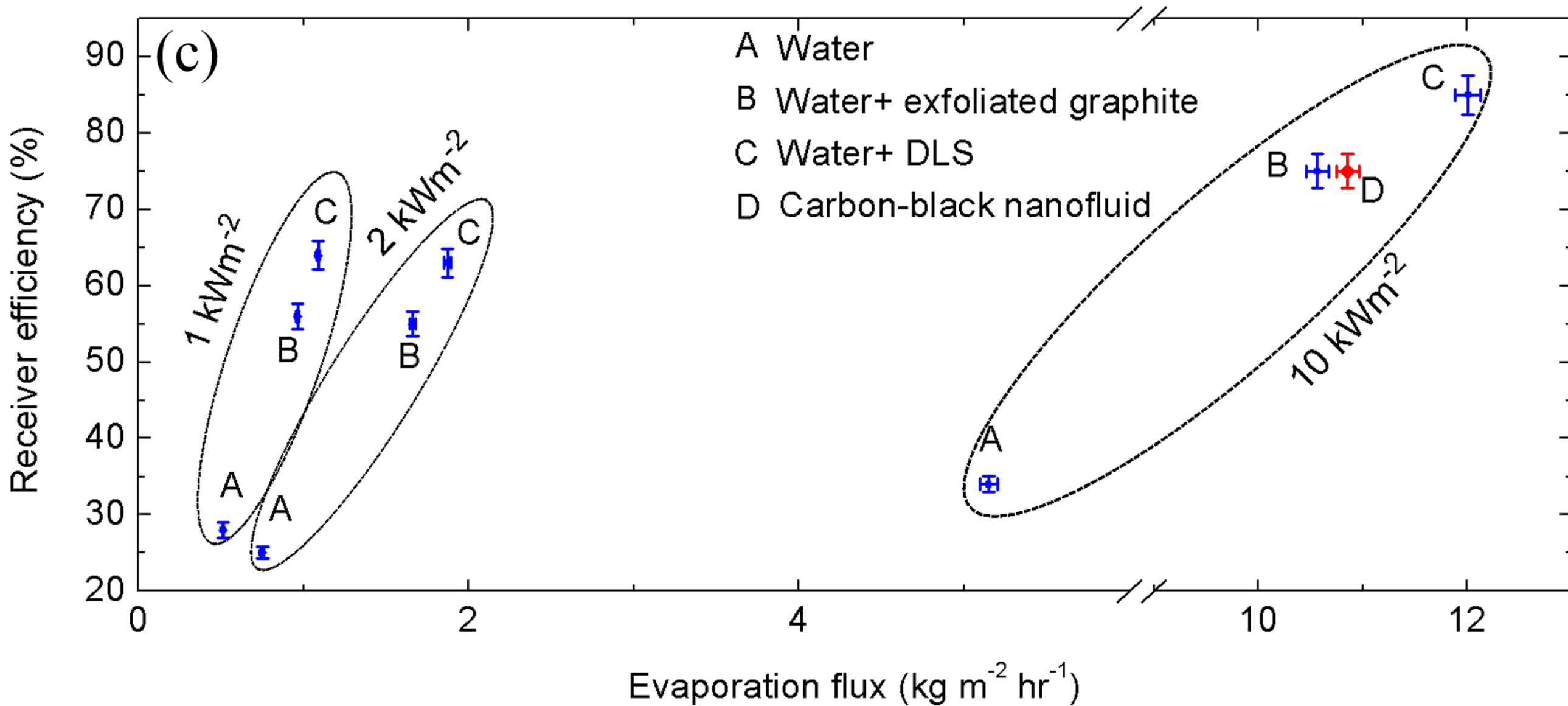
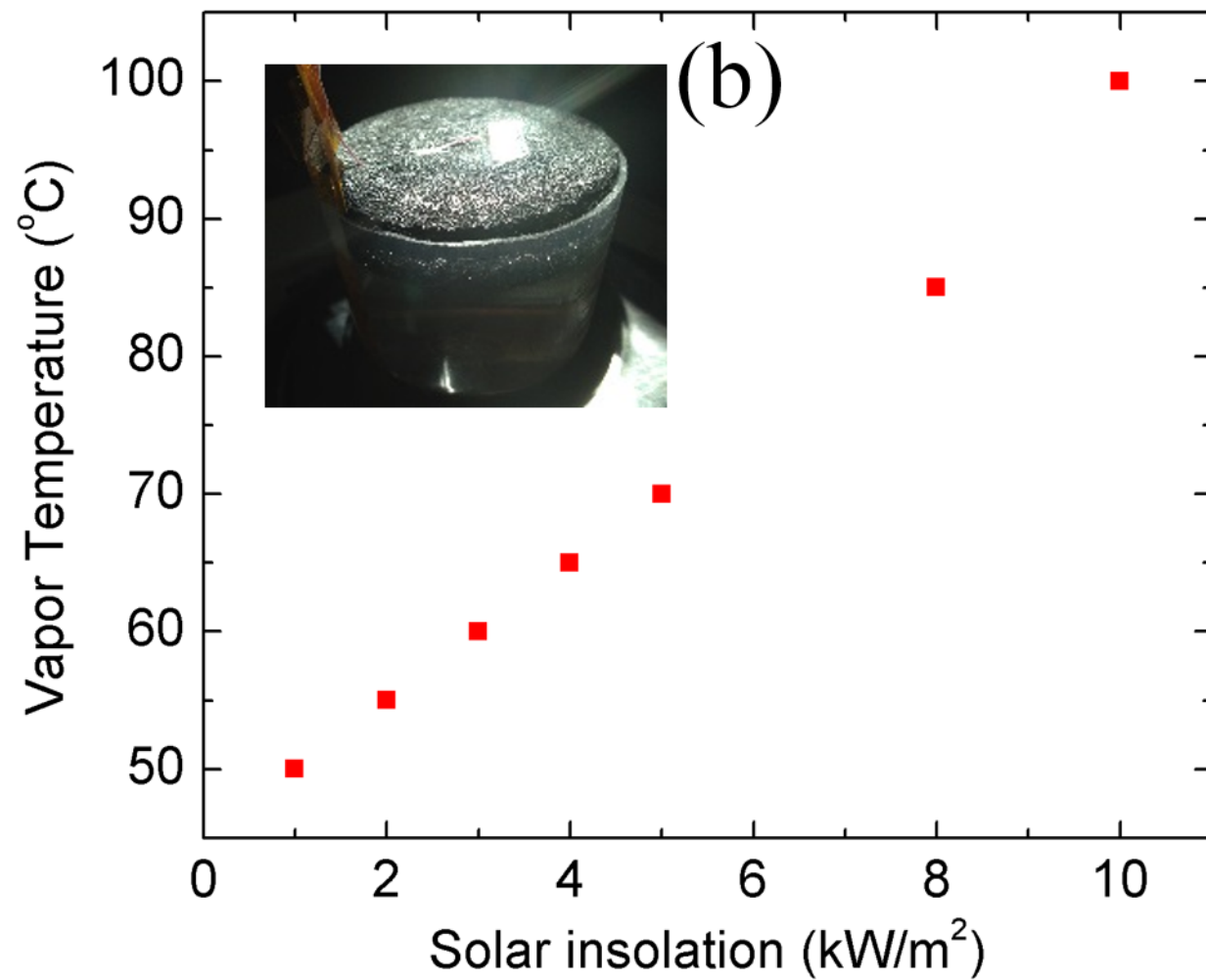
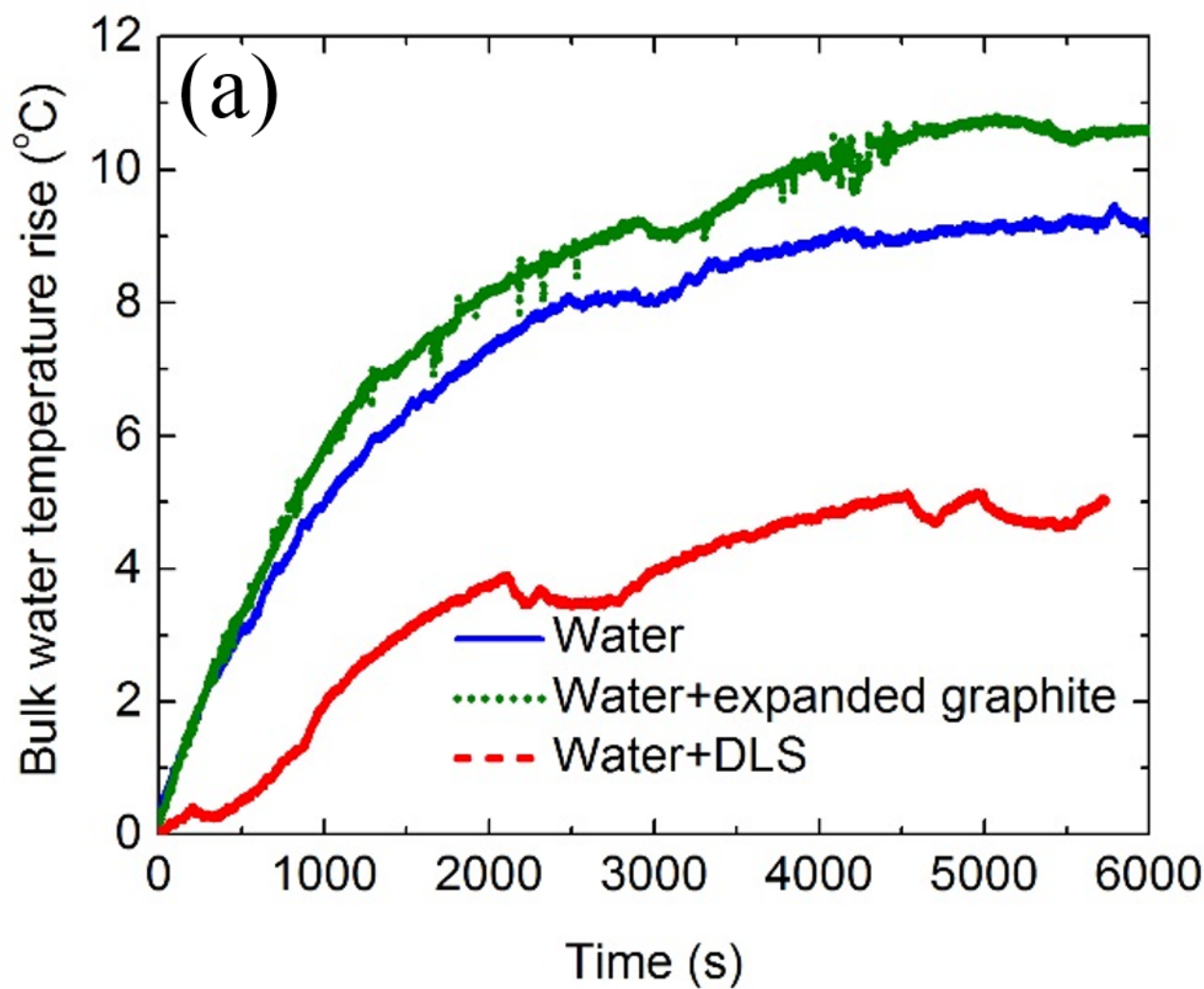
Exfoliated graphite
(absorbing, hydrophilic & porous)

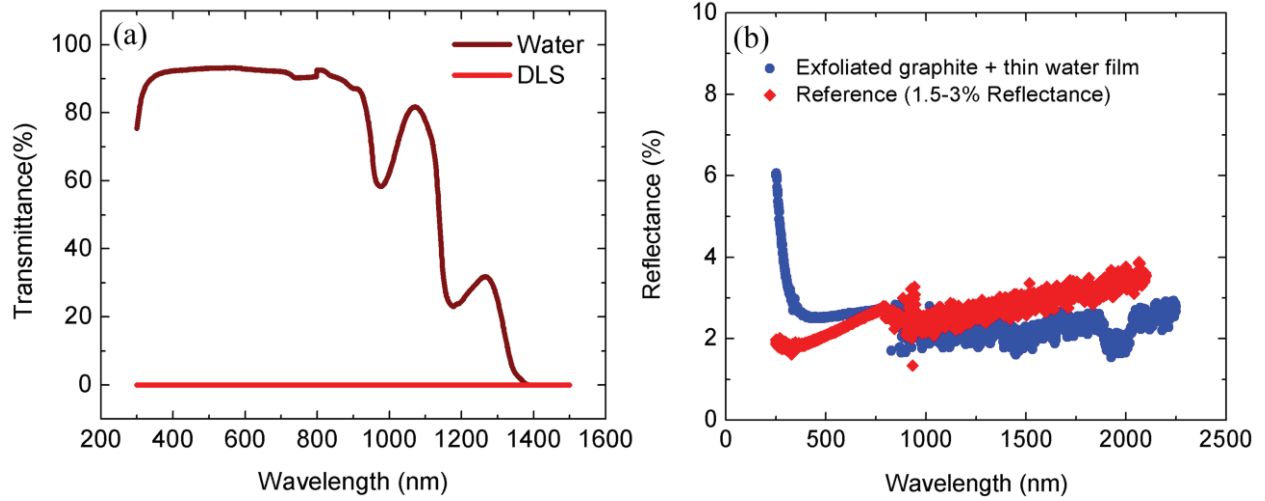
Carbon foam
(insulating, hydrophilic & porous)



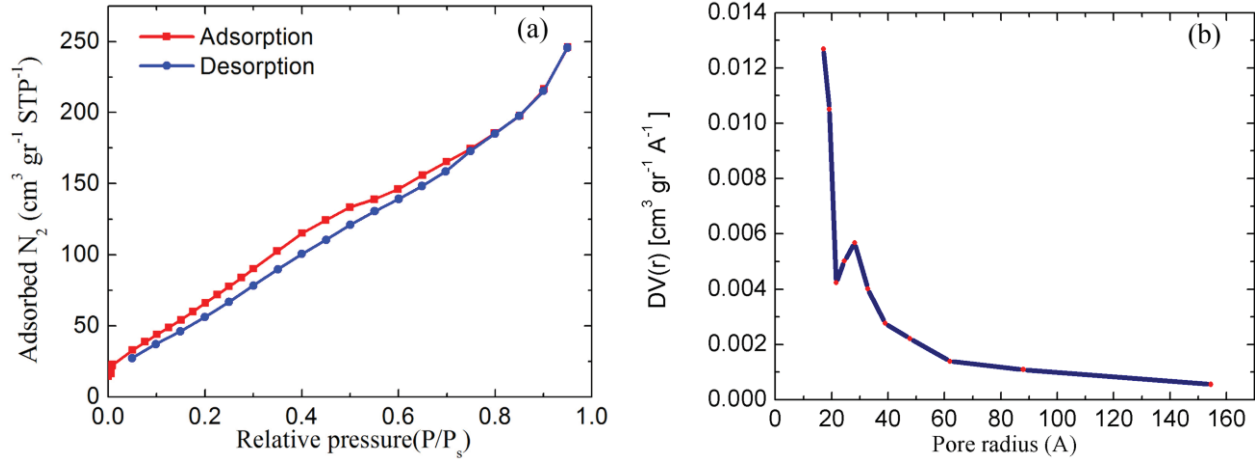




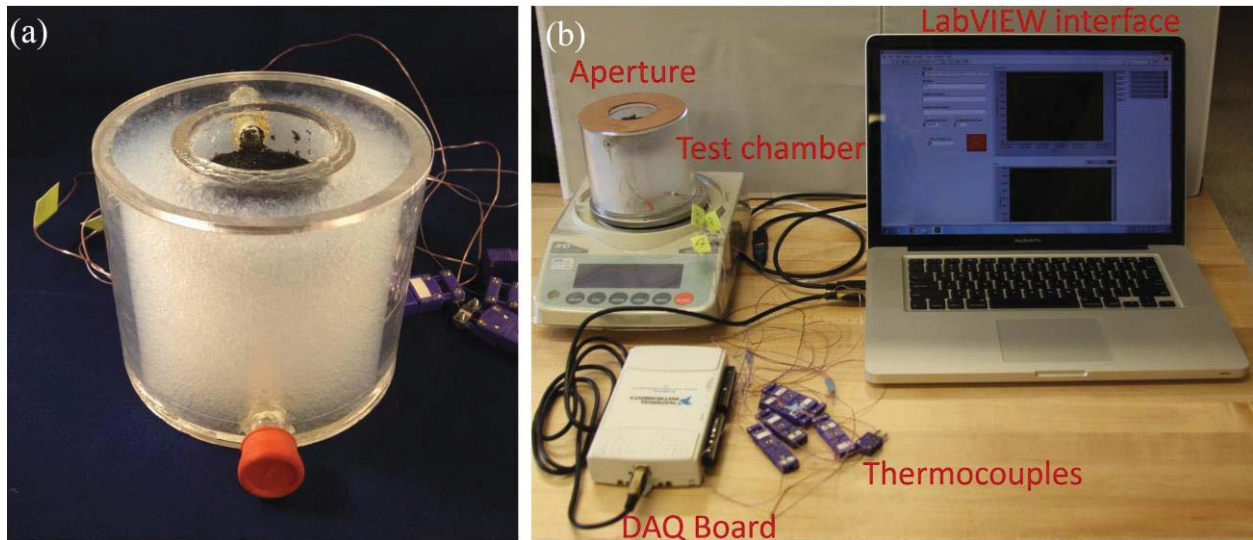




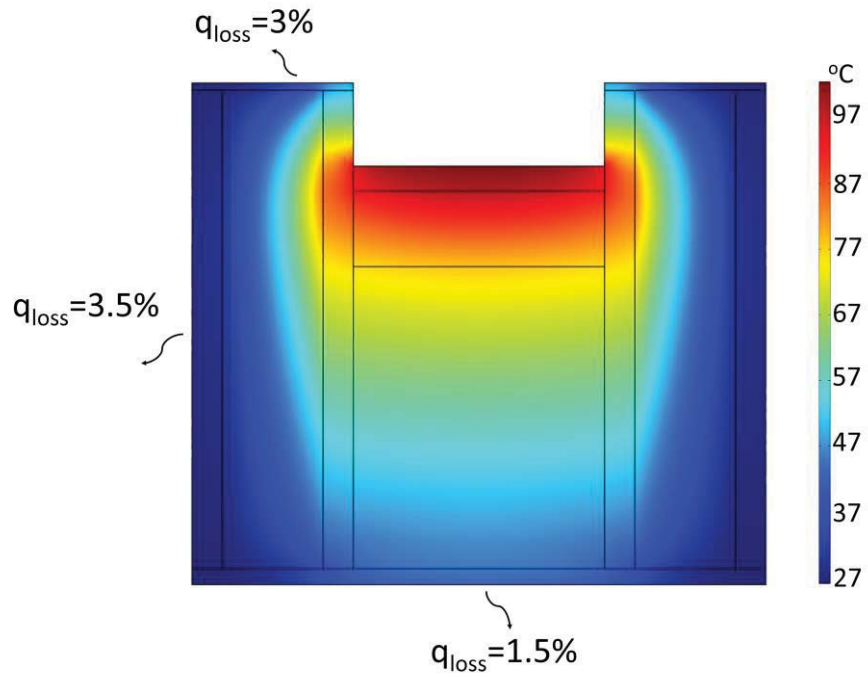
Supplementary Figure 1| Optical properties of the DLS. (a) The transmittance of water and the DLS in the wavelength range of 300-1500 nm (b) the reflectance of the DLS structure in the wavelength range of 250-2250 nm including both diffusive and specular reflectance. The reference sample was obtained from Avain Technologies LLC (FGS-02-02c; Fluorilon Gray Standard).



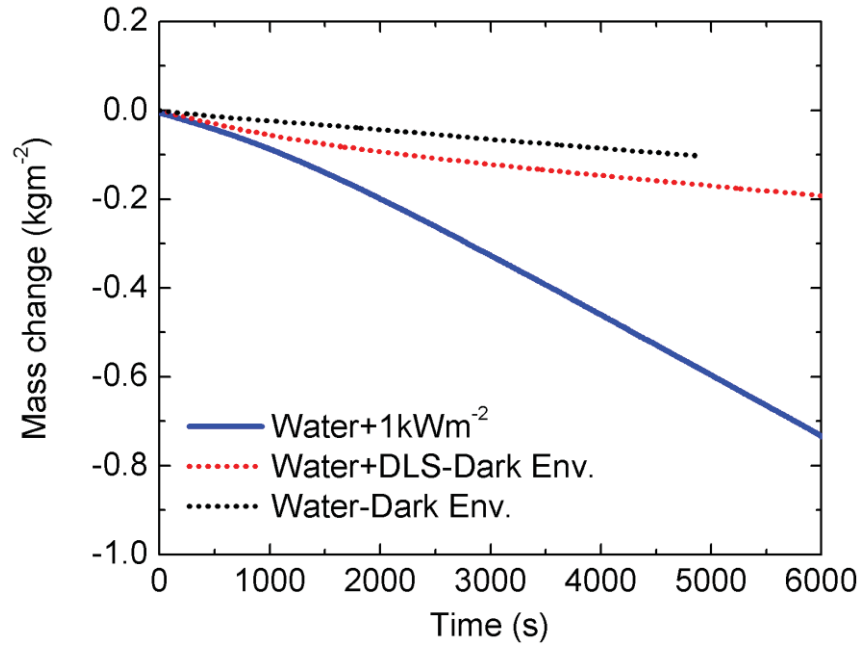
Supplementary Figure 2 | Surface characteristics of the exfoliated graphite. (a) The adsorption- desorption isotherm of N₂ at 77 K on exfoliated graphite. The BET surface area of this structure is 320 m²g⁻¹ indicating 32 times enhancement in the exfoliation process. (b) The pore size distribution of exfoliated graphite determined by the BJH model.



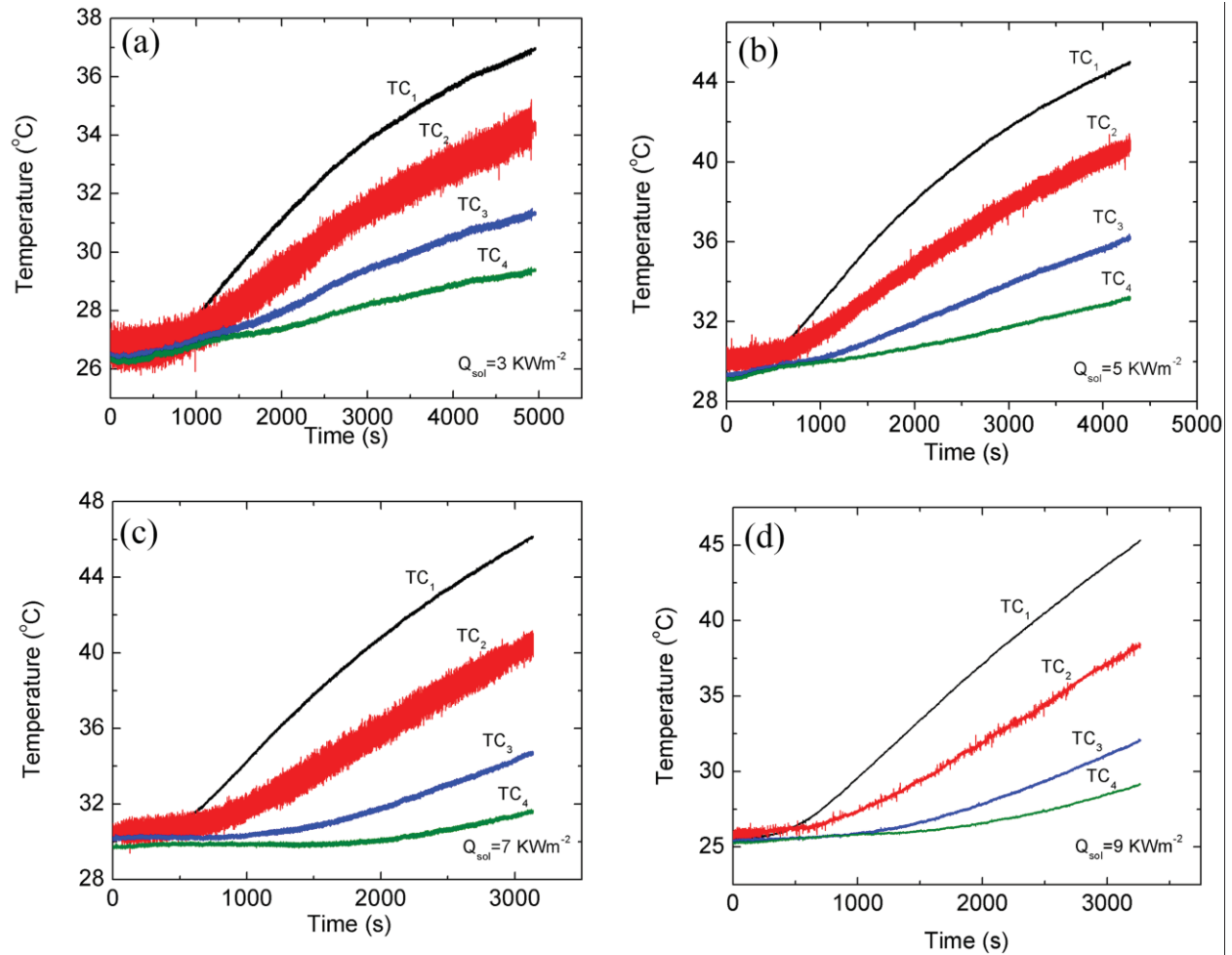
Supplementary Figure 3| The experimental set-up. (a) Test chamber designed to minimize side losses (b) The evaporation rate and temperature field in the liquid and vapor phases are measured and the data are collected with a DAQ board controlled by a LabVIEW interface.



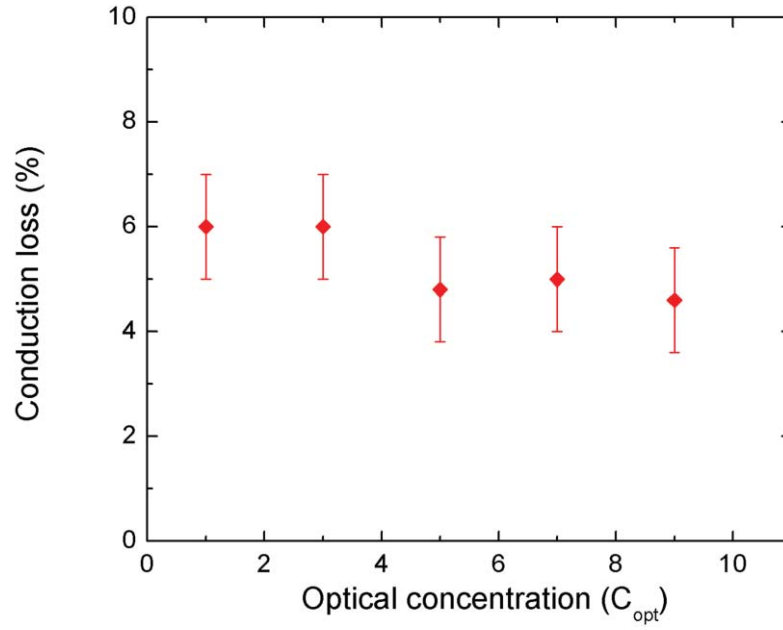
Supplementary Figure 4| Simulated thermal losses of the test chamber. Thermal losses of the test chamber is simulated by COMSOL under a solar irradiation of 10 kWm^{-2} . The boundary conditions of the walls are convective heat fluxes with a coefficient of $5 \text{ Wm}^{-2}\text{K}^{-1}$.



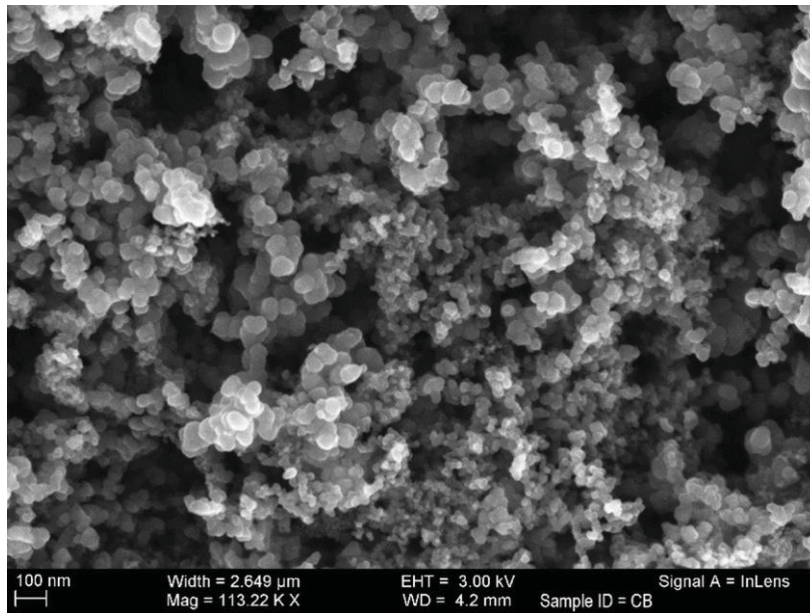
Supplementary Figure 5| Evaporation under dark condition. The evaporation rate of water under dark conditions and under solar irradiation of 1 kWm⁻². The absorption of water and its temperature increase causes a significant enhancement in evaporation.



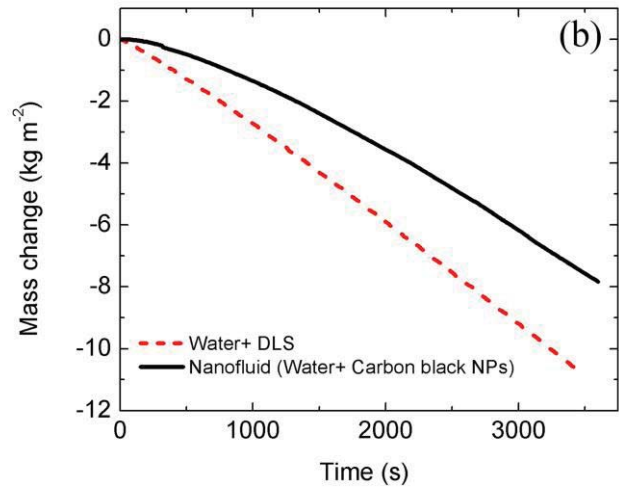
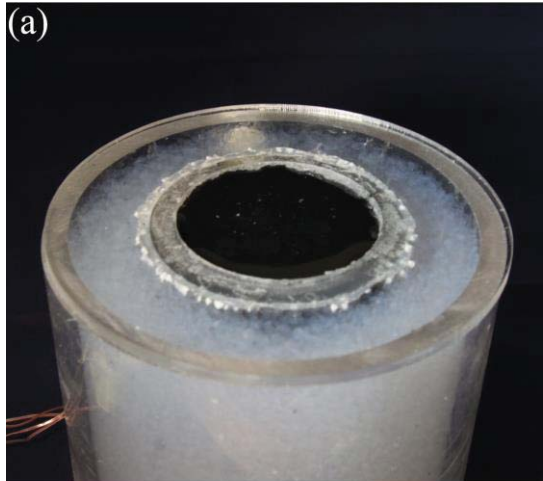
Supplementary Figure 6 | Temperature gradient in the underlying fluid. The temperature gradient in the underlying water below the DLS is measured with four embedded thermocouples in the test chamber. The distance between the thermocouples is 10 mm. The gradient between the top two thermocouples is used to calculate heat conduction losses to the underlying water.



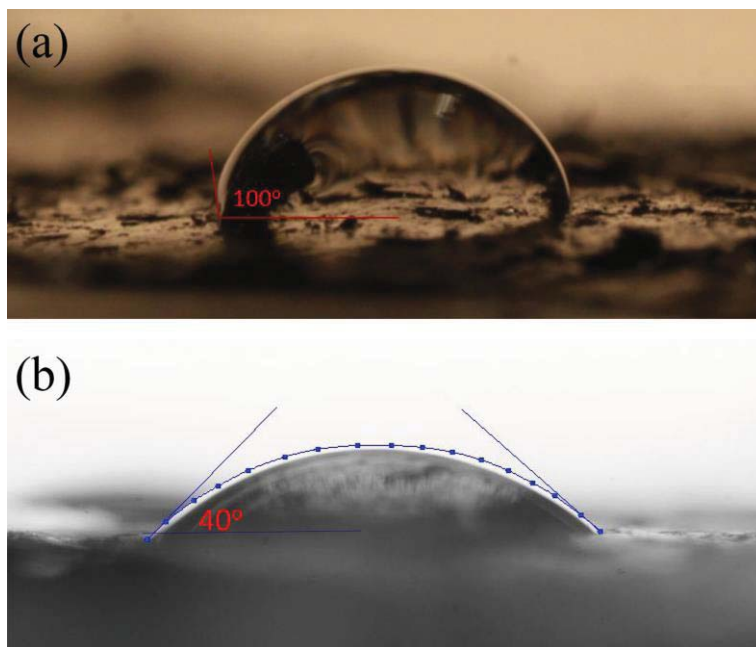
Supplementary Figure 7| Conduction losses. Heat conduction losses of the DLS to underlying water as a function of optical concentration are measured.



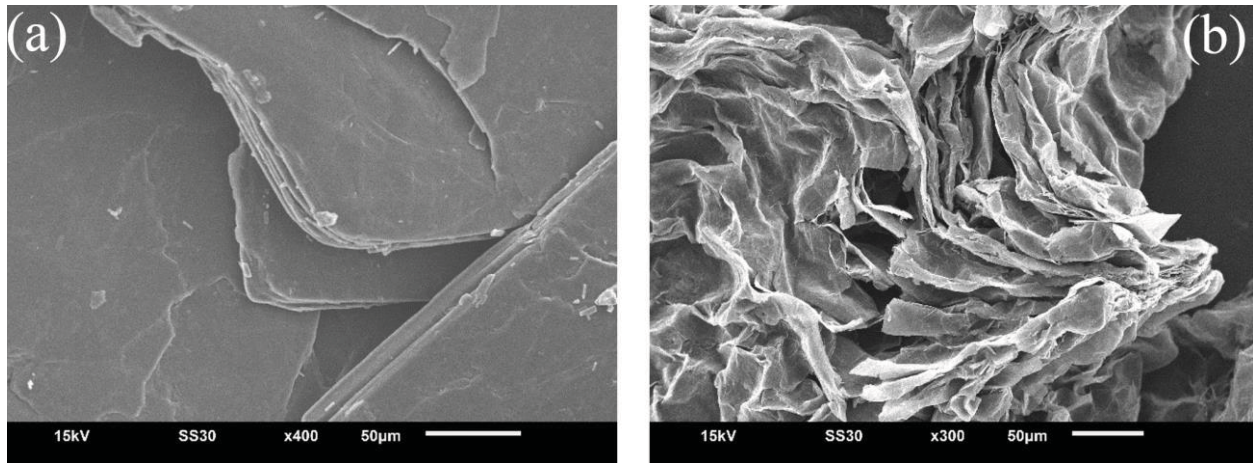
Supplementary Figure 8| Carbon black nanoparticles. The microstructure of the carbon black NPs used in the nanofluid receiver. The concentration of these particles is 0.5 wt% in the solution.



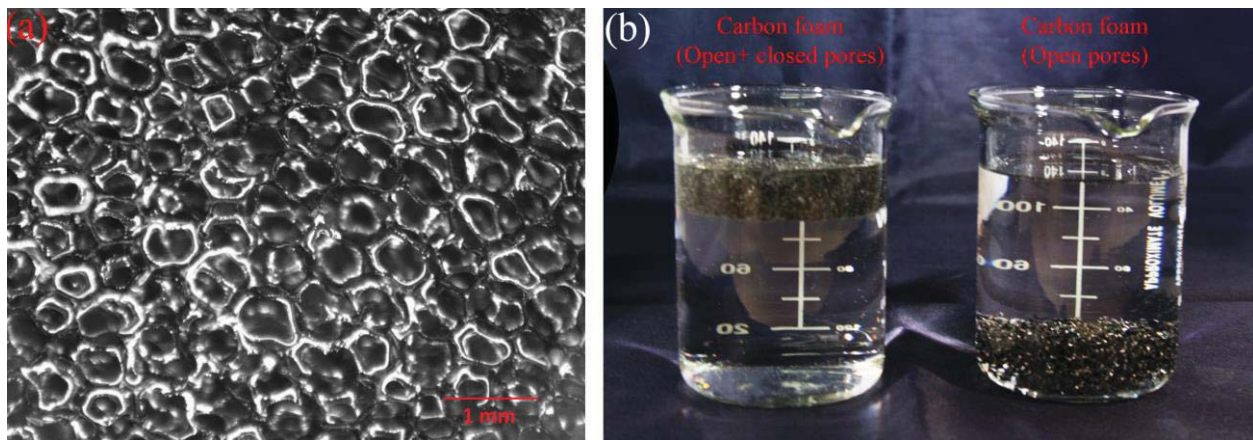
Supplementary Figure 9 | Nanofluid solar receiver. (a) The experimental setup with carbon black nanofluid (b) The vapor generation rate by the nanofluid and the DLS are compared. The DLS shows higher steam temperature, higher efficiency and faster dynamics.



Supplementary Figure 10| Contact angle of water on graphite flakes. (a) Thin film of as-washed graphite flakes and (b) exfoliated graphite. Although the graphite flakes possess hydrophobic surfaces (contact angle of $100\pm 2^\circ$), the exfoliated graphite flakes show hydrophilic surface (contact angle of $40\pm 2^\circ$).



Supplementary Figure 11| Microstructure of graphite flakes. (a) Before microwave exfoliation and (b) after exfoliation for 7s. The exfoliation process causes formation of a porous interconnected structure.



Supplementary Figure 12| Characteristics of the carbon foam. (a) The microstructure of the carbon foam. Diameter of the pores are in the range of 300-600 μm . (b) The left subfigure shows the carbon foam consisting of both closed and open pores floating on top of the water surface while in the right-hand side subfigure, the carbon foam comprising of only open pores sinks in the water.

Supplementary Note 1| Optical properties of the DLS. The optical transmission spectrum of carbon foam, exfoliated graphite and pure water are measured in the wavelength range of 300-1500 nm, (Supplementary Fig. 1a). For both carbon foam and exfoliated graphite (DLS), the transmittance is less than 0.01%. The reflectance of the exfoliated graphite is measured with Cary 500i UV-VIS-NIR Dual-Beam Spectrophotometer including an integrating sphere (diffusive and specular reflectance) in the wavelength range of 250-2250 nm and is shown in (Supplementary Fig. 1b). The error in the measurements is $\pm 1\%$. The reflectance measurements cover approximately the entire AM 1.5G solar spectrum. The portion of solar irradiation in the wavelength range of 2250-2900 nm is $\sim 0.2\%$. This reflection along with transmittance results suggests that $97\pm 1\%$ of solar energy is absorbed in the exfoliated graphite layer.

Supplementary Note 2| Surface area of exfoliated graphite. The surface area of the exfoliated graphite is measured by N_2 adsorption experiments at 77K (Quantachrome, Autosorb-iQ). The adsorption-desorption curves are shown in (Supplementary Fig. 2a). The Brunauer-Emmett-Teller (BET) model suggests the surface area of $320 \text{ m}^2\text{g}^{-1}$ for exfoliated graphite while the surface area of graphite flakes is only $10 \text{ m}^2\text{g}^{-1}$ before exfoliation by microwave radiation. The 32 times enhancement in the surface area is caused by exfoliation of graphite flakes in the microwave process. The pore size distribution in the exfoliated graphite is determined using the BJH model and shown in (Supplementary Fig. 2b). Most of the pores have a radius of $< 6\text{nm}$. Note that these pores are within each particle of the exfoliated graphite. The spacing between particles is on the order several hundred micrometer.

Supplementary Note 3| The experimental setup. The experimental setup is shown in (Supplementary Fig. 3). The setup is equipped with a solar simulator (Newport 94082A), power measuring system (including Newport thermopile detector (818P-040-55, 40W, 55 mm diameter) and Newport power meter (1918-c)), a test chamber, balance, DAQ board, and data collection system.

The designed test chamber is shown in (Supplementary Fig. 3a). The test chamber consists of two concentric acrylic tubes with inside diameters of 50 mm and 100 mm and height of 96 mm. The gap between the tubes is filled with translucent hydrophobic aerogel particles (Cabot Lumira LA 1000 Aerogel, 700 μm -4 mm diameter, Aerogel Technologies) to minimize side losses. Based on the COMSOL simulations in (Supplementary Note 4), the parasitic losses of the test chamber are $\sim 6.5\%$ (3% top surface and 3.5% side walls) of total solar illumination. Four T-type thermocouples are embedded in the inside tube with 10 mm intervals. These thermocouples are used to measure the heat conduction loss to the underlying water. The thermocouples are calibrated with an accuracy of 0.1 K prior to experiments. Another thermocouple is placed on top of the DLS to measure the temperature of the generated steam at the surface of the structure. The thermocouple is coated with a highly reflective white Boron Nitride coating (Cotronic corporation) to suppress the heating effect of direct illumination on the thermocouple reading.

The illumination source is a solar simulator (Newport 94082A) with an optical filter for AM 1.5G spectrum. This simulator uses a xenon lamp and proprietary filter to meet Class A performance parameters without compromising the 1 sun output power. This solar simulator has $< 2^\circ$ collimated output. The temporal non-uniformity of the illuminated beam is $\pm 2\%$. The reported spatial uniformity of the illuminated beam by the manufacturer is $\pm 5\%$. The solar illumination of the solar simulator is reflected by metal mirror angled 45° onto a rectangular

polymer Fresnel lens ($17.5 \times 17.5 \text{ cm}^2$). A copper aperture with diameter of 50 mm is placed below the Fresnel lens and above the test chamber to form a circular solar illumination spot with the same diameter of the inside tube of test chamber. The solar irradiation is measured at the level of the DLS with the power measurement system. The Newport thermopile detector has a larger diameter (55 mm) than the solar illumination spot. The total power is measured with the thermopile detector and is divided by the area of the copper aperture to determine the solar illumination flux. The non-uniformity of the solar illuminated spot is determined by measuring the solar illumination with a smaller Newport thermopile detector (818P-001-12) at eight points along the diameter of the solar spot. At an average concentration of 10 kWm^{-2} , the local solar flux varies from 8-12 kWm^{-2} . The balance is used to monitor the mass loss from evaporation, and consequently determine the efficiency of solar-thermal conversion.

Supplementary Note 4| Simulation of heat losses. We simulated the thermal losses of the test chamber in a steady state condition in COMSOL, neglecting the fluid motion (which is small in the liquid). The boundary conditions for the test chamber are as follows: convective boundary condition with $h=5 \text{ Wm}^{-2}\text{K}^{-1}$ at the walls and top and bottom surface of the test chamber excluding the evaporating surface. At the evaporation surface, an evaporation heat transfer coefficient of $120 \text{ Wm}^{-2}\text{K}^{-1}$ was determined by matching the COMSOL absorber temperature with the measured vapor temperature. This evaporation heat transfer coefficient is a conservative approximation due to volumetric characteristics of the absorber. A boundary heat flux of 10 kWm^{-2} (10 suns) was applied at the absorber top surface. The exfoliated graphite layer is

approximately 5mm thick, and has a thermal conductivity of $0.93 \text{ Wm}^{-1}\text{K}^{-1}$ (as measured in (Supplementary Fig. 3)). The carbon foam is 12 mm thick, and has a thermal conductivity of $0.43 \text{ Wm}^{-1}\text{K}^{-1}$. The thermal conductivity of the walls (acrylic) and aerogel insulation are considered $0.2 \text{ Wm}^{-1}\text{K}^{-1}$ and $0.02 \text{ Wm}^{-1}\text{K}^{-1}$, respectively. The cross-sectional temperature field in the test chamber is shown in (Supplementary Fig. 4). The heat losses from the side walls and the top surface is shown in the figure. Due to lab-scale size of the test chamber, 6.5% of the parasitic losses are caused by the top surface (3%) and side walls (3.5%). Note that although thermal conductivity of the side walls (Acrylic+ Silica aerogel) is less than water, due to higher surface area of the walls, thermal losses of the side walls are more than the bottom surface. That is, the DLS promises higher values of receiver efficiency in large-scale 1-D structures.

Supplementary Note 5| Evaporation rate of pure water. The evaporation rates of water in a dark environment and under solar irradiation of 1 kWm^{-2} are measured at the same ambient temperature and humidity. The water evaporation rate in a dark environment is $74 \text{ kgm}^{-2}\text{hr}^{-1}$ (only 15% of that under solar illumination of 1 kWm^{-2}), (Supplementary Fig. 5). The evaporation rate in the dark condition is subtracted from all the measured data under the solar illumination. The absorptance of pure water in the visible and infrared regime throughout the volume causes an enhanced evaporation compared to the dark environment. We conducted these measurements to exclude the role of ambient condition and humidity on our measurements. We note that in the literature this effect is neglected and the reported efficiencies include both solar irradiation and ambient condition effects.

Supplementary Note 6| Conduction losses. The conduction loss to the underlying water is calculated using the temperature gradient in the underlying water. Once the vapor temperature at the surface of the DLS reaches to a steady-state condition, the temperature gradient in the underlying water is measured. (Supplementary Fig. 6) shows the temperature vs. times at different locations in the underlying water (TC_1 is just below the DLS, and the interval between thermocouples are 10 mm) for optical concentrations of 3, 5, 7, and 9. These temperature gradients are used to calculate the heat conduction losses to the underlying liquid, (Supplementary Fig. 7).

Supplementary Note 7| Nanofluid based solar receiver. A nanofluid solution was prepared using carbon black NPs (Cabot, Vulcan 9) in a concentration of 0.5 wt% in deionized water. The solution was sonicated for one hour to make a uniform solution. The microstructure of the NPs is shown in (Supplementary Fig. 8). The particle diameters are in the range of 20-60 nm. We measured the absorption of this nanofluid with Cary 500i UV-Vis-NIR Dual-Beam Spectrophotometer in the wavelength range of 250-2250 nm. The solution has absorption of >99% in this wavelength range. This nanofluid is utilized in the experimental setup as discussed above for solar steam generation. The experimental and measurement procedure was same as the one reported above, (Supplementary Fig. 9a). The vapor generation rate as a function of time for this nanofluid receiver is compared with the DLS and shown in (Supplementary Fig. 9b).

The generated vapor temperature by this nanofluid under solar irradiation of 10 kWm^{-2} is $\sim 80^\circ\text{C}$ (compared to DLS $\sim 100^\circ\text{C}$) and the receiver efficiency at this solar concentration is $75\pm 3\%$ while this efficiency for the DLS is $85\pm 3\%$. Compared to the DLS, nanofluid solar receiver leads

to both lower vapor temperature and lower receiver efficiency. The major source of low efficiency is conducted heat from the liquid-vapor interface to the bulk nanofluid. In the DLS, heat is localized at the liquid-vapor interface and the conduction loss to the bulk fluid is minimized.

Furthermore, we have compared the performance of the DLS as a solar receiver with other current technologies as reported in¹, Fig. 5d. These technologies include selective surfaces, nanofluid, and PS10 volumetric receiver (wire mesh). These performances are calculated for a receiver in a solar tower collector. All these systems are non-vacuum. Note that no optical concentration losses are considered in these efficiencies. The reported intrinsic efficiencies are plotted as a function of $(T_{\max}-T_{\text{am}})/C_{\text{opt}}$ where T_{\max} denotes the maximum temperature of working fluid in the receiver and T_{am} the ambient temperature. Normally, for flat-panel solar collectors, the figure of merit is defined as $(T_{\text{avg}}-T_{\text{am}})/C_{\text{opt}}^2$ where T_{avg} is

$$T_{\text{avg}} = \frac{(T_{\text{in}} + T_{\text{out}})}{2}$$

T_{in} and T_{out} denote inlet and outlet temperature of working fluid, respectively. Since the DLS is designed to generate high temperature working fluid while keeping the bulk fluid cold, for a better comparison herein with the DLS, we have used T_{\max} in the figure of merit formula rather than T_{avg} . Note that using T_{avg} in the figure of merit formula is in favor of the DLS in the comparison. As shown, the DLS shows higher performance than the current systems at low optical concentrations and offers a new approach for efficient solar-thermal harvesting.

Supplementary Note 8| Hydrophilic nature of the DLS. The porous structure of the DLS promotes the fluid flow through capillary force if it is hydrophilic. This force depends on the contact angle of the fluid on the surface of the porous structure. If the surface is hydrophobic, it adversely affects the evaporation rate. The contact angle of water on graphite flakes and exfoliated graphite are measured and shown in (Supplementary Fig. 10). In both cases, a thin slab of the graphite is fabricated by pressing at a pressure of 13.5 MPa for 12 hrs. The contact angle of water on graphite flakes is $100\pm 2^\circ$, and $40\pm 2^\circ$ for exfoliated graphite.

Supplementary Note 9| Microstructure of graphite flakes and carbon foam. Microstructures of graphite flakes before and after microwave exfoliation are shown in (Supplementary Fig. 11). The volumetric expansion (~ 100 times) in the microwave detaches the graphite flakes and forms a highly porous structure with 32 times higher surface area than acid-washed graphite flakes. The second component of the DLS is the carbon foam. As discussed, the carbon foam utilized in this work consists of both open and closed pores. A microstructure of this foam is shown in (Supplementary Fig. 12a). The pore diameters are in the range of 300-600 μm . In an ideal case, the size of open pores should balance the capillary pressure and flow viscous pressure in the foam structure. This leads to maximum temperature in the structure without drying out.

The closed pores in the carbon foam structure lead to float of this structure on top of the water surface. This characteristic is shown in (Supplementary Fig. 12b) on the left-hand side subfigure. The vertical position of the carbon foam floating on the surface suggests that the density of foam

is close to density of water. If the foam only consists of open pores, it will sink in the water as shown in the (Supplementary Fig. 12b), right-hand side subfigure.

Supplementary Note 10| Potential application of the DLS. Although at early stage, we envision that efficient solar steam generation with the DLS has many potential applications, some examples are given below.

1. Processes that involve evaporation of pure liquid including power generation, some distillation processes, absorption chillers, mixed-fluid waste treatment and solar ponds. Solar ponds are used for mineral extraction, hazardous waste treatment and agricultural water treatment. Fast and efficient evaporation in these ponds has both economic (fast processing) and environmental (land use) advantages.
2. Processes that involve evaporation of liquid solution including desalination, some sterilization approaches, and chemical purification. The evaporated liquid leaves solid particles in the absorbing structure and leads to fouling phenomenon. This phenomenon is an intrinsic problem to membrane-based desalination systems. The current solutions for this problem are described in chapter 15 of the reference³ with the title of “Membrane elements fouling and performance restoration”. Briefly, the solutions are back washing or chemical treatment. The carbon foam is treated with 4% molar nitric acid during preparation stage with no detectable change in the properties, suggesting its chemical stability.

3. Our current system is not pressurized. In a pressurized system, we expect to achieve higher pressure and temperature for potential power generation applications.

Supplementary references

1. Taylor, R. a. *et al.* Applicability of nanofluids in high flux solar collectors. *J. Renew. Sustain. Energy* **3**, 023104 (2011).
2. Del Col, D., Padovan, A., Bortolato, M., Dai Prè, M. & Zambolin, E. Thermal performance of flat plate solar collectors with sheet-and-tube and roll-bond absorbers. *Energy* **58**, 258–269 (2013).
3. Wilf, M. *The Guidebook to Membrane Desalination Technology: Reverse Osmosis, Nanofiltration and Hybrid Systems; Process Design, Applications and Economics.* (Balaban Desalination Publications, 2007).